JOURNAL OF GEOPHYSICAL RESEARCH, VOL. 113, B05305, doi:10.1029/2007JB004981, 2008

Heterogeneous coupling of the Sumatran megathrust constrained by geodetic and paleogeodetic measurements

M. Chlieh,[1,2] J. P. Avouac,[1] K. Sieh,[1] D. H. Natawidjaja,[1,3] and John Galetzka[1]

Received 8 February 2007; revised 12 November 2007; accepted 23 January 2008; published 13 May 2008.

[1] Geodetic and paleogeodetic measurements of interseismic strain above the Sumatran portion of the Sunda subduction zone reveal a heterogeneous pattern of coupling. Annual banding in corals provides vertical rates of deformation spanning the last half of the 20th century, and repeated GPS surveys between 1991 and 2001 and continuous measurements at GPS stations operated since 2002 provide horizontal velocities. Near the equator, the megathrust is locked over a narrow width of only a few tens of kilometers. In contrast, the locked fault zone is up to about 175 km wide in areas where great interplate earthquakes have occurred in the past. Formal inversion of the data reveals that these strongly coupled patches are roughly coincident with asperities that ruptured during these events. The correlation is most spectacular for rupture of the M_w 8.7 Nias-Simeulue earthquake of 2005, which released half of the moment deficit that had accumulated since its previous rupture in 1861, suggesting that this earthquake was overdue. Beneath the Mentawai islands, strong coupling is observed within the overlapping rupture areas of the great earthquakes of 1797 and 1833. The accumulated slip deficit since these events is slowly reaching the amount of slip that occurred during the 1833 earthquake but already exceeds the slip that occurred during the 1797 earthquake. Thus, rerupture of part of the Mentawai patch in September 2007 was not a surprise. In contrast, coupling is low below the Batu islands near the equator and around Enggano island at about 5°S, where only moderate earthquakes ($M_w < 8.0$) have occurred in the past two centuries. The correlation of large seismic asperities with patches that are locked during the interseismic period suggests that they are persistent features. This interpretation is reinforced by the fact that the large locked patches and great ruptures occur beneath persistent geomorphologic features, the largest outer arc islands. Depth- and convergence-rate-dependent temperature might influence the pattern of coupling, through its effect on the rheology of the plate interface, but other influences are required to account for the observed along-strike heterogeneity of coupling. In particular, subduction of the Investigator Fracture Zone could be the cause for the low coupling near the equator.

Citation: Chlieh, M., J. P. Avouac, K. Sieh, D. H. Natawidjaja, and J. Galetzka (2008), Heterogeneous coupling of the Sumatran megathrust constrained by geodetic and paleogeodetic measurements, *J. Geophys. Res.*, *113*, B05305, doi:10.1029/2007JB004981.

1. Introduction

[2] Slip along a subduction megathrust results from a combination of aseismic and seismic slip. Steady aseismic slip becomes dominant at depths greater than about 40–50 km, whereas great megathrust earthquakes result from rupture of patches at shallower depths [*Mazzotti et al.*, 2000; *Pacheco et al.*, 1993; *Ruff and Kanamori*, 1983; *Savage*, 1983; *Tichelaar and Ruff*, 1993]. In order for elastic strain to build up and be released during interplate earthquakes, the subduction megathrust must be wholly or partially locked during the interseismic period so that a slip deficit accumulates. Some correlation between the spatial distribution and amount of slip deficit accumulating in the interseismic period and interplate seismic slip is therefore expected. This is the relationship investigated in this study, which focuses on the Sumatran segment of the Sunda megathrust.

[3] It is already known that seismic slip is spatially heterogeneous [*Dmowska et al.*, 1996; *Ji et al.*, 2002; *Kanamori*, 1986; *Subarya et al.*, 2006; *Thatcher*, 1990; *Yamanaka and Kikuchi*, 2004]. Nonetheless, we still

[1]Tectonics Observatory, Division of Geological and Planetary Sciences, California Institute of Technology, Pasadena, California, USA.
[2]Now at Géosciences Azur, Université de Nice Sophia-Antipolis, Institut de Recherche pour le Développement, Observatoire de la Côte d'Azur, Valbonne, France.
[3]Now at Research Center for Geotechnology, Indonesian Institute of Sciences, Bandung, Indonesia.

0148-0227/08/2007JB004981$09.00

understand poorly how aseismic and seismic interplate slip sum to produce a spatially uniform slip rate in the long run.

[4] Here, we characterize the locking of the shallow portion of the megathrust by its degree of 'interseismic coupling,' a ratio that we define as v/v_0, where v is the slip rate deficit along the megathrust and v_0 is the long-term slip rate required by plate convergence (an interseismic coupling of 1 thus corresponds to full locking). This use is consistent with previous literature and is a purely kinematic quantity, not a direct reflection of mechanical coupling related to the stress distribution on the megathrust. We use another term, 'seismic coupling,' to refer to the ratio of the accumulated seismic moment released by a number of large megathrust earthquakes over a given period, divided by the moment which should have been released assuming that slip at depth shallower than the downdip end of the seismogenic zone (taken to be 40 km here) is only seismic and amounts to that computed from the long-term slip rate. Over the long run, these two quantities should be equal if 'interseismic' refers to the whole period between successive megathrust ruptures (including postseismic and eventual preseismic slip associated with the megathrust events). They might be estimated locally, or, as is more common practice, as a regional average for a particular megathrust. Measurements of interseismic strain across various megathrusts have revealed a wide range of interseismic coupling, from complete locking of the shallow megathrust (<40–50 km depths) to nearly total decoupling [*Bürgmann et al.*, 2005; *Chlieh et al.*, 2004; *Cross and Freymueller*, 2007; *Dragert et al.*, 1994; *Fletcher et al.*, 2001; *Fournier and Freymueller*, 2007; *Freymueller and Beavan*, 1999; *Mazzotti et al.*, 2000; *Wallace et al.*, 2004; *Wang et al.*, 2003]. Along-strike variations in coupling may result from complex interactions between intrinsic structural or rheological characteristics of the subduction system including sedimentary cover, fracture zones and landforms on the subducting plate. In addition, interseismic coupling is time-dependent. Interplate ruptures may trigger aseismic slip on adjacent parts of the megathrust [*Chlieh et al.*, 2004; *Heki and Tamura*, 1997; *Hsu et al.*, 2006; *Hutton et al.*, 2001; *Pritchard and Simons*, 2006; *Zweck et al.*, 2002] and transient spontaneous aseismic events are also common [*Dragert et al.*, 2001; *Hirose et al.*, 1999; *Lowry et al.*, 2001; *Wallace and Beavan*, 2006]. Such transient slow event was reported from the Sumatran section of the Sunda subduction zone in 1962 to have a source dimension equivalent to a seismic rupture of about magnitude (M_w) 8.4 [*Natawidjaja et al.*, 2007].

[5] Thus, understanding better the processes of heterogeneous strain accumulation and release is a major issue with important implications for both earthquake physics and seismic hazard assessment. More specific questions are these: How do the dimensions of locked fault patches compare to the areas that rupture during large earthquakes? Are such seismic asperities permanent features associated with local properties of the megathrust? Does the moment release during one particular seismic event equal the moment deficit accumulated since the previous rupture of that same patch? These questions have been investigated in a number of previous studies but are still mostly unresolved [e.g., *Aoki and Scholz*, 2003; *Bürgmann et al.*, 2005; *Dmowska and Lovison*, 1992; *Kanamori*, 1977; *Lay et al.*, 1989; *Park and Mori*, 2007; *Thatcher*, 1990].

[6] For several reasons, Sumatra is a particularly appropriate place to investigate these questions (Figure 1). First, we know relatively well the coseismic slip distribution of the great 2004 Sumatra-Andaman (M_w 9.15) and the 2005 Nias-Simeulue (M_w 8.7) ruptures from geodetic and seismologic constraints [*Ammon et al.*, 2005; *Banerjee et al.*, 2005; *Briggs et al.*, 2006; *Chlieh et al.*, 2007; *Konca et al.*, 2007; *Rhie et al.*, 2007]. Second, analyses of growth patterns within coral microatolls have revealed vertical interseismic displacements of the past 50 years [*Natawidjaja et al.*, 2007; *Natawidjaja et al.*, 2004; *Sieh et al.*, 1999; *Zachariasen et al.*, 2000] and vertical displacements associated with great intraplate earthquakes in 1797 and 1833 and a moderate earthquake in 1935 [*Natawidjaja et al.*, 2006; *Natawidjaja et al.*, 2004; *Rivera et al.*, 2002]. Third, GPS campaigns in the 1990s [*Bock et al.*, 2003; *McCaffrey et al.*, 2000; *Prawirodirdjo et al.*, 1997] and continuous monitoring by the Sumatran GPS Array (SuGAr) since 2002 document recent interseismic strain (http://www.tectonics.caltech.edu/sumatra/data.html).

[7] First, we introduce the kinematic framework of the Sumatran plate boundary. Then we present the data sets we will use and our modeling strategy. Finally, we discuss the pattern of coupling along the plate interface and how it relates to seismicity, in particular to the rupture areas of the 1935 earthquake and the great 1797, 1833, 2005, and 2007 earthquakes.

2. Secular Motion and Megathrust Geometry

2.1. Secular Motion

[8] The Sumatran section of the Sunda subduction zone is a classic example of slip partitioning [*Fitch*, 1972; *McCaffrey*, 1991; *McCaffrey et al.*, 2000]. Oblique subduction of the Australian plate beneath the Sunda block separates almost completely into dip slip along the Sunda megathrust, which crops out on the seafloor at the Sunda trench, and dextral trench-parallel strike slip along the Sumatran fault (Figure 2). The Sunda block rotates anticlockwise relative to Australia at an angular velocity of 0.68°/Ma around a pole located at 129.2°W and 7.9°S, near the East Pacific ridge (Table 1) [*Bock et al.*, 2003]. The velocity of the Sunda plate relative to Australia increases southward across Sumatra from ~56 mm/a to ~62 mm/a (black arrows in Figure 2). Other plate models for the Sumatran plate boundary yield about the same relative motion [*Michel et al.*, 2001; *Simons et al.*, 2007; *Simons et al.*, 1999; *Socquet et al.*, 2006].

[9] It seems reasonable to assume that the long-term slip rate of the subduction megathrust equals the component of the relative plate motion that is parallel to the slip vectors of megathrust earthquakes [*McCaffrey*, 1991]. This leaves a residual component of right-lateral motion parallel to the Sumatran fault. Between these two principal elements of the plate boundary is a narrow fore-arc sliver, which we presume to be rigid (Figure 2). This is only a first-order kinematic description, because internal deformation of the sliver exists [*Bellier and Sebrier*, 1995; *Diament et al.*, 1992; *McCaffrey*, 1991; *Sieh and Natawidjaja*, 2000].

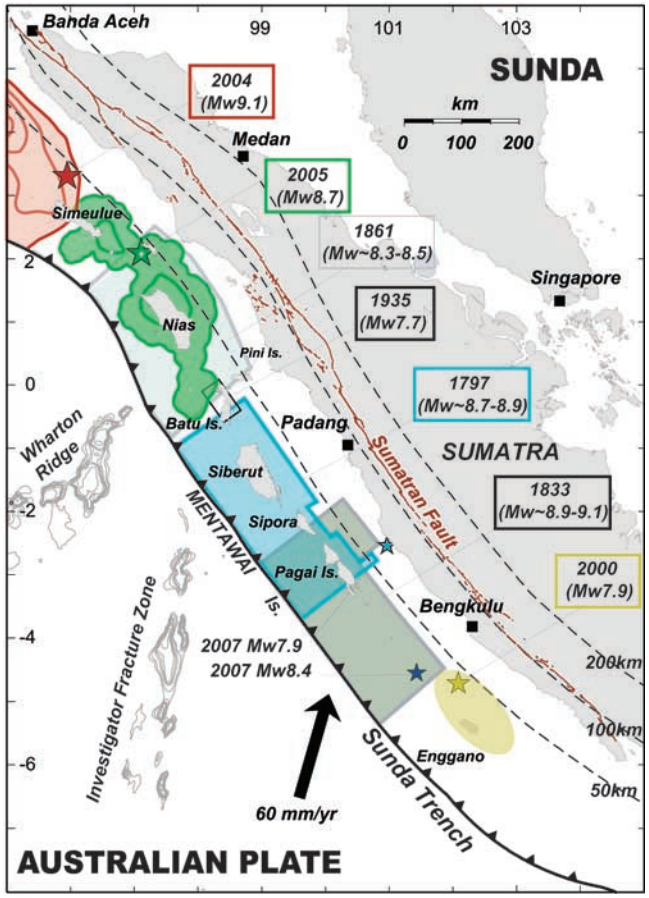

Figure 1. Basic active structural elements and historical great earthquakes of the obliquely convergent Sumatran plate boundary. Green and red 5-m contour lines of slip for the 2004 Sumatra-Andaman and 2005 Nias-Simeulue earthquakes are from *Chlieh et al.* [2007] and *Briggs et al.* [2006], respectively. Outermost contours depict the limits of rupture. Approximate rupture area of the $M_w \sim 8.3-8.5$ 1861 earthquake is based on macroseismic effects [*Newcomb and McCann*, 1987]. Ruptures during the great 1797 and 1833 earthquakes are from elastic dislocation models based on uplift of coral microatolls [*Natawidjaja et al.*, 2006]. The magnitude (M_w) is reestimated assuming a layered 1-D CRUST2.0 structure. The southern limit of the 1833 rupture is poorly constrained. The ellipse shows the approximate rupture of the 2000 earthquake and the relatively high seismic activity that occurred in this area in the last decade from *Abercrombie et al.* [2003]. Epicenters of the 2007 M_w 8.4 South Pagai and the M_w 7.9 Pagai-Sipora earthquakes are shown for reference (http://earthquake.usgs.gov/eqcenter/). Dashed lines parallel to the trench are the 50, 100, and 200 km depth of the megathrust [*Gudmundsson and Sambridge*, 1998].

[10] Since our objective is to understand motions on the megathrust, we are interested in the relative motion of the fore-arc sliver relative to the Australian plate, which we deduce by subtracting out strike-slip motion across the Sumatran fault. To do this, we calculate the pole of rotation of the fore-arc sliver relative to the Sunda block by minimizing normal motion across the Sumatran fault. A pole of rotation in southeast Africa yields the best fit to purely dextral strike-slip motion across the Sumatran fault (Table 1 and red arrow in Figure 2). The angular velocity about this pole should yield a slip rate on the Sumatran fault that in turn results in motion between the fore-arc sliver and Australia plates (yellow arrow in Figure 2) parallel to the megathrust slip vectors deduced from the Harvard CMT Catalogue covering the period 1976–2005. The angular velocity of the fore-arc sliver thus derived is 0.22°/Ma anticlockwise. This yields a rate of about 23 mm/a on the Sumatran fault, a value consistent with geological estimates near and north of the equator, but double the tentative geological estimates south of the equator [*Bellier and Sebrier*, 1995; *Sieh and Natawidjaja*, 2000]. This slip rate compares well with velocities derived from triangulation survey and GPS transects across the Sumatran fault around 1°N and 3°S [*Genrich et al.*, 2000; *Prawirodirdjo et al.*, 2000]. In this kinematic model, the long-term convergence between the fore-arc sliver and Australia is nearly perpendicular to the trench and varies from 41 mm/a at about 2°N to 48 mm/a at 7°S (Figure 2).

2.2. Megathrust Geometry and Modeling of Interseismic Strain

[11] In the absence of strong local constraints on the geometry of the megathrust, we define a three-dimensional geometry based on bathymetry, global catalogs of seismicity and focal mechanisms (Figure 3). The curved geometry of the interface is adjusted through trench-normal cross sections to fit the locations of hypocenters from the relocated ISC catalog for the period 1964–1998 and dip angle indicated by the focal mechanisms of interplate earthquakes [*Engdahl et al.*, 1998]. The dip of the slab interface is about 5°–7° close to the trench, and increases gradually from 15°–20° below the Mentawai Islands to 30° below the coastline of Sumatra. The geometry is smoothly interpolated both along dip and strike, with nodes every 5 km. This is the geometry used in the case of the forward modeling approach described below in section 4.2. For the formal inversion models described in sections 4.3 to 4.5, we have simplified the megathrust geometry to a rectangular dislocation starting at the trench with a uniform dip of 13°. The proposed megathrust geometry is consistent with the 13° dip angle beneath Nias Island derived from finite source modeling of the 2005 Nias earthquake [*Konca et al.*, 2007]. This dip could be as much as 5° too high along the shallow portion of the megathrust, but this is unimportant, since the data do not help to resolve well that portion of the megathrust anyway. Sensitivity tests to the megathrust dip described in Appendix A show that a 13° ± 3 dipping slab provides the best fits to the data.

[12] Commonly, interseismic strain is modeled using the theory of dislocations embedded in an elastic half-space. Assuming that the hanging wall does not deform over the long term, a back-slip modeling approach is reasonable [*Savage*, 1983]. The idea is that interseismic strain can be represented by the superposition of strain due to sliding along the megathrust at the long-term secular rate and strain due to backward slip, at a rate equal to or smaller than the long-term slip rate, on the

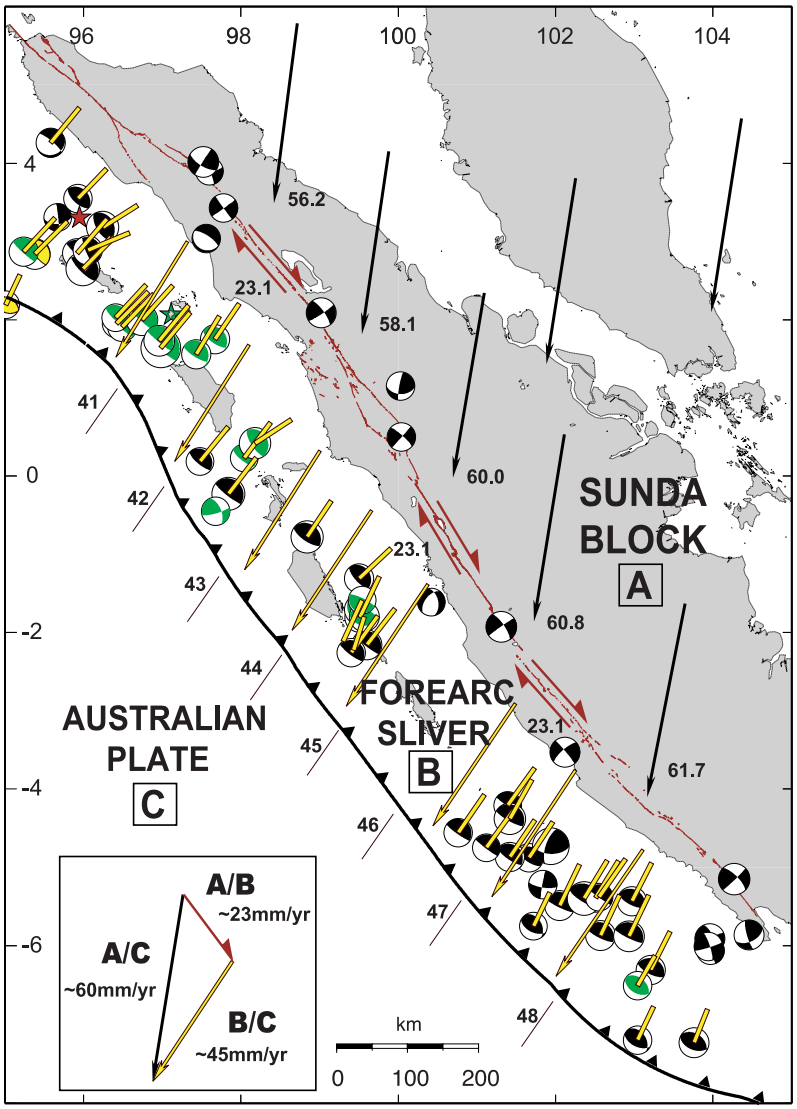

Figure 2. Plate tectonic setting of the study area. Secular motion of the Sunda block (A) and fore-arc sliver (B) relative to Australian plate (C), indicated by arrows with rates in mm/a. Relative motion of Sunda block (A) relative to the Australian plate (C) is from *Bock et al.* [2003]. Plate motion of the fore-arc sliver was determined by assuming that its motion relative to Australian plate is parallel to slip vectors of moderate interplate earthquakes along the Sumatra megathrust. The fore-arc sliver's motion relative to the Sunda block is parallel to the Sumatran fault and about 23 mm/a. Resulting horizontal motion of the fore-arc sliver relative to the Australian plate is about 45 mm/a trenchward. Focal mechanisms are from the Harvard centroid moment tensor (CMT) catalog for earthquakes with $M_w > 6$ between 1976 and June 2005 (http://www.seismology.harvard.edu/CMTsearch.html). Focal mechanisms of earthquakes posterior to the M_w 8.7 March 2005 Nias-Simeulue earthquake are shown in green.

patches that are locked during the interseismic period. If strain due to the secular motion is assumed to be nil, only the back-slip term needs to be modeled. When the megathrust cannot be assumed to be a planar surface, the back-slip model is only a first-order approximation, since the strain due to the secular motion modeled from a forward slipping dislocation would not be null [*Vergne et al.*, 2001]. It follows that if the megathrust were fully locked, the downdip end of the back-slip surface would only need to coincide with the downdip end of the locked fault zone and be locally tangent to the megathrust [*Vergne et al.*, 2001]. If the megathrust is only partially

Table 1. Plate Velocities as Rotation of the First-Named Plate Relative to the Second-Named Plate[a]

Block Pair	Longitude, °E	Latitude, °N	Ω, °/Ma	Reference
Sund/ITRF2000	−95.9	49.4	0.32 ± 0.01	*Bock et al.* [2003]
Aust/ITRF2000	38.1	33.0	0.62 ± 0.00	*Bock et al.* [2003]
Sund/Aust	−129.19	−7.91	0.68	This Study
Sund/Sliv	33.0	−32.0	−0.22	This Study
Sliv/Aust	−122.6	−22.8	0.54	This Study

[a]Sund, (Sunda Block); Aust, (Australia); Sliv, (Sumatra fore-arc sliver). Sund/Aust was computed by combining poles derived relative to ITRF2000 from *Bock et al.* [2003]. Sund/Sliv is proposed for this study by minimization of normal deformation across the Sumatran fault and Sliv/Aust is deduced from the two previous (Figure 2).

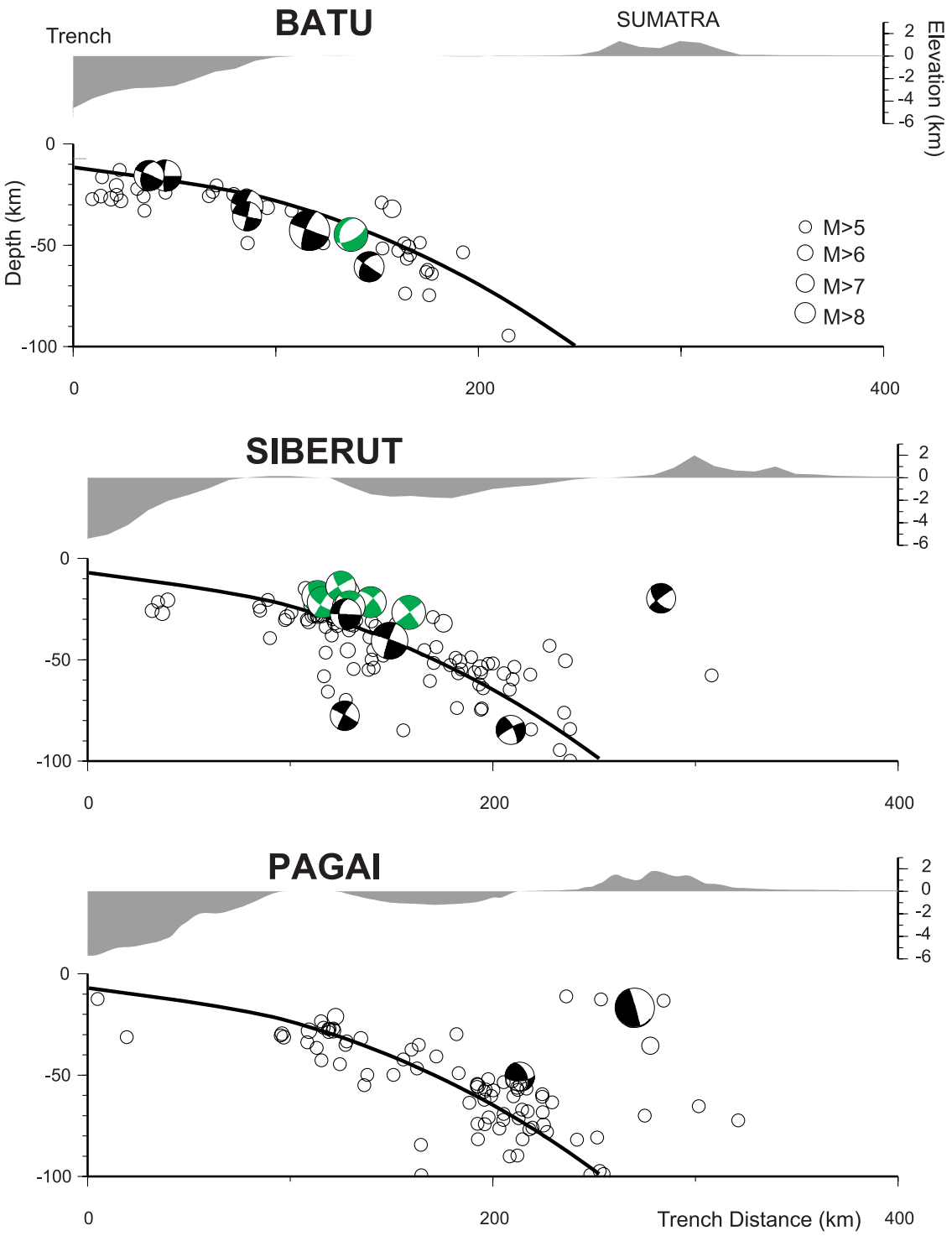

Figure 3. Topography, relocated seismicity [*Engdahl et al.*, 1998], the focal mechanisms, and the proposed geometry of the megathrust along trench-normal sections across the Batu, Siberut, and Pagai islands.

locked then the geometry of the back-slip model needs to coincide with the real megathrust.

3. Paleogeodetic and Geodetic Data

[13] For this study, we have compiled 110 paleogeodetic and geodetic measurements of interseismic deformation. This data set includes estimates of subsidence and uplift rates from coral growth (Figure 4), horizontal velocities derived from survey mode GPS measurements, and horizontal and vertical velocities derived from continuous GPS (CGPS) measurements (Figure 5). Tables 2, 3, and 4 list these velocities and their assigned 1σ uncertainties.

3.1. Paleogeodetic Records

[14] We use vertical displacement rates estimated from coral growth rings for the period between 1962 and 2000 at 44 sites (Table 2). The basis for all these measurements is described in *Natawidjaja et al.* [2004] for the Batu islands and *Natawidjaja et al.* [2007] for Siberut, Sipora, and the Pagai islands. Most of the data are from sites 100 to 150 km from the trench (Figure 4). Three sites (Telur, Angsa, and Tikos) are farther east, near the mainland coast of Sumatra, about 200 km from the trench.

[15] To estimate geodetic subsidence (or uplift), we correct the coral vertical growth rates by a rate of global sea level rise of 1.8 mm/a. This correction was chosen on the basis of the time-averaged rate of 1.5 ± 0.5 mm/a estimated from global tide gauge records over the last century and 2.8 ± 0.4 mm/a recorded by TOPEX/Poseidon and Jason altimeter satellites over the period 1993–2003 [*Cazenave and Nerem*, 2004; *Church and White*, 2006].

[16] Although the paleogeodetic time series show significant temporal variations, we focus here on the long-term average rates, deferring the analysis of the temporal variations to ongoing studies [*Kositsky et al.*, 2006]. Averaged vertical velocities range from a maximum uplift rate of 5.6 mm/a at Tanjung Anjing, in the Batu islands (∼120 km from the trench) to a subsidence rate of 12.3 mm/a at Masokut island, just south of Siberut island (∼100 km from the trench).

[17] Graphs of vertical rates drawn along lines perpendicular to the trench (Figure 4b) show high subsidence rates that decrease away from the trench, uplift at distances between ∼100–120 km and ∼150 km, and no net uplift nor subsidence along the coast of the Sumatra mainland, about 200 km from the trench. This pattern is consistent with that expected from simple models in which some portion of the shallow megathrust is locked during the interseismic period [*Natawidjaja et al.*, 2004; *Sieh et al.*, 1999].

[18] For reference, we compare these coral data with predicted uplift rates computed by assuming that the plate interface is fully locked from the trench to a depth of either 30, 40 or 50 km, corresponding to locked fault zone widths of ∼110, 150, or 200 km (Figure 4b and models F-a, F-b, F-c in Table 5). We use *Okada*'s [1992] analytical solution for a dislocation in an elastic half-space and *Savage's* [1983] back-slip approach, assuming a back-slip velocity vector consistent with the long-term velocity vector determined from the secular model of section 2 (Figure 2). The paleogeodetic data thus imply that a significant fraction of the megathrust must have remained locked over the period 1962–2000. The downdip end of the locked fault zone must lie about 150 to 200 km from the trench south of the equator (Figure 4b, Siberut and Sipora-Pagai sections) and about 130 km from the trench near the equator (Batu section). The paleogeodetic data have the potential to provide constraints on the degree of coupling of the plate interface and possible lateral variations of the width of the locked fault zone.

3.2. Survey Mode GPS and Permanent GPS

[19] We use velocities from 33 sites surveyed during GPS campaigns between 1991 and 2001 (Table 3) from *Bock et al.* [2003]. These survey mode GPS data cover a broader area than the paleogeodetic data, and the spatial coverage is better in the north than in the south (Figure 5a). Velocities at continuous GPS (CGPS) stations of the Sumatran GPS Array (SuGAr), installed by the Caltech Tectonics Observatory (http://www.tectonics.caltech.edu/sumatra/data.html) from September 2002 onward were also integrated into this analysis. Six of these stations were operating for 2 years before the December 2004 Sumatra-Andaman earthquake, so their pre-December 2004 horizontal velocities (green arrows in Figure 5a) help in estimation of the pattern of slip deficit on the locked fault zone. The displacements recorded by the International GNSS Service (IGS) stations near the city of Medan (SAMP) and at Nanyang Technololgical University in Singapore (NTUS) were incorporated into this analysis, as well.

[20] We also used velocities determined from post-2005 measurements (June 2005 to October 2006) at 17 stations south of the equator, where no significant postseismic response occurred. These data were first analyzed separately to estimate the state of the locked fault zone after the occurrence of the two great earthquakes of December 2004 and March 2005, then jointly with the coral and GPS campaigns measurements. Stations within about 100 km of the 2004 and 2005 ruptures were not used in this analysis, because they continue to show the influence of postseismic afterslip on the megathrust.

[21] The data were processed by SOPAC (http://sopac-devel.ucsd.edu/projects/sugar.html) with the GAMIT/GLOBK software (http://www-gpsg.mit.edu/∼simon/gtgk/) [*Herring*, 2000; *King and Bock*, 2000] and analyzed in 24-h segments with data from 10 additional continuous GPS sites on Java, Cocos Islands, Diego Garcia, Singapore, India, Australia, and Guam. These solutions were combined with global GPS network solutions produced routinely at the Scripps Orbit and Permanent Array Center (http://sopac.ucsd.edu) to determine the secular velocities and their uncertainties with respect to the ITRF2000 reference frame [*Altamimi et al.*, 2002] using the procedure of *Nikolaidis* [2002]. The velocities at the continuous GPS sites (green arrows in Figure 5a) are consistent with those determined at nearby sites from campaign measurements (black arrows).

[22] Velocities referenced to the Australian plate (using the Australian plate motion of *Bock et al.* [2003]) decrease gradually trenchward, a pattern consistent with some degree of locking of the megathrust. The velocities decrease from about 61 mm/a at NTUS (Singapore) to 15–30 mm/a on the Mentawai islands (Figure 5). Three monuments east of the Sumatran fault (Blms, Duri and Pasi) show azimuths at odds with velocities determined from IGS stations at SAMP and NTUS or computed from the plate motion of Sunda relative to Australia (Figure 5a). These anomalous vectors might reflect slip on local active secondary structures in the back-arc region, or be an artifact related to the short period between occupations in 1991 and 1993. These three stations, which are too far from the trench to be sensitive to coupling on the megathrust interface were excluded from the modeling.

[23] The decrease of horizontal velocities toward the trench is generally consistent with the downdip end of the locked portion of the plate interface lying between 110 and 200 km away from the trench (Figure 5b). The large velocities at the Batu island stations (near the equator)

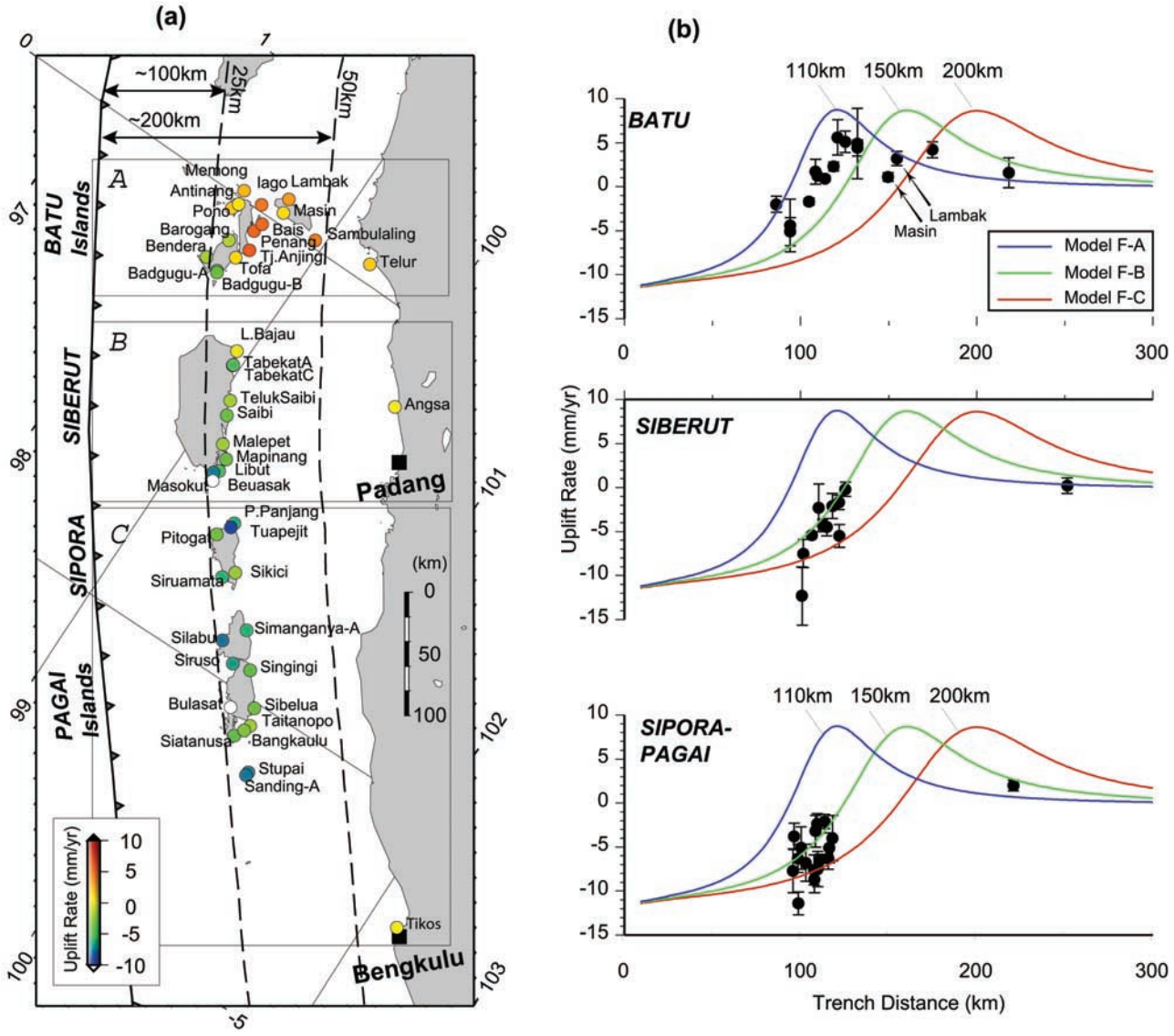

Figure 4. Vertical displacement rates determined from coral growth over the period 1962–2000 (Table 2) (a) in map view and (b) along sections normal to the trench [*Natawidjaja et al.*, 2007; *Natawidjaja et al.*, 2004]. Boxes A, B, and C in Figure 4a indicate the swath corresponding to each section. The origin of horizontal axis for each section is at the trench. Outer arc islands are subsiding, a pattern consistent with the interseismic locking of the shallow portion of the plate interface. Continuous lines in Figure 4b show theoretical uplift rates predicted by assuming that the plate interface is fully locked from the trench down to a depth of either 30, 40, or 50 km, corresponding to a horizontal width of the locked fault zone of 110, 150, or 200 km, respectively (forward models F-a, F-b, and F-c in Table 5). Subsidence rates increase southward along strike suggesting that the locked fault zone gets wider to the south.

and Enggano (at about 5°S) imply less coupling there than at higher latitudes.

4. Modeling

4.1. Assumptions and Strategy

[24] We assume that the pattern of interseismic strain revealed by the geodetic and paleogeodetic data depends only on the spatial distribution of coupling along the megathrust, with purely elastic deformation of the overlying and subducting plate. We therefore neglect any contributions of nonelastic deformation in the fore arc during the interseismic period. Although there is evidence for some deformation of the fore arc, this seems a reasonable assumption given that the cumulative deformation recorded since the mid-Holocene yield millennial rates of vertical deformation about an order of magnitude smaller than interseismic rates [*Zachariasen*, 1998]. Finally, we assume that the secular velocities are constant. We will see that this first-order approximation allows reasonable reconciliation of the coral data (1962–2000), the campaign GPS measurements from the 1990s and the more recent SuGAr CGPS

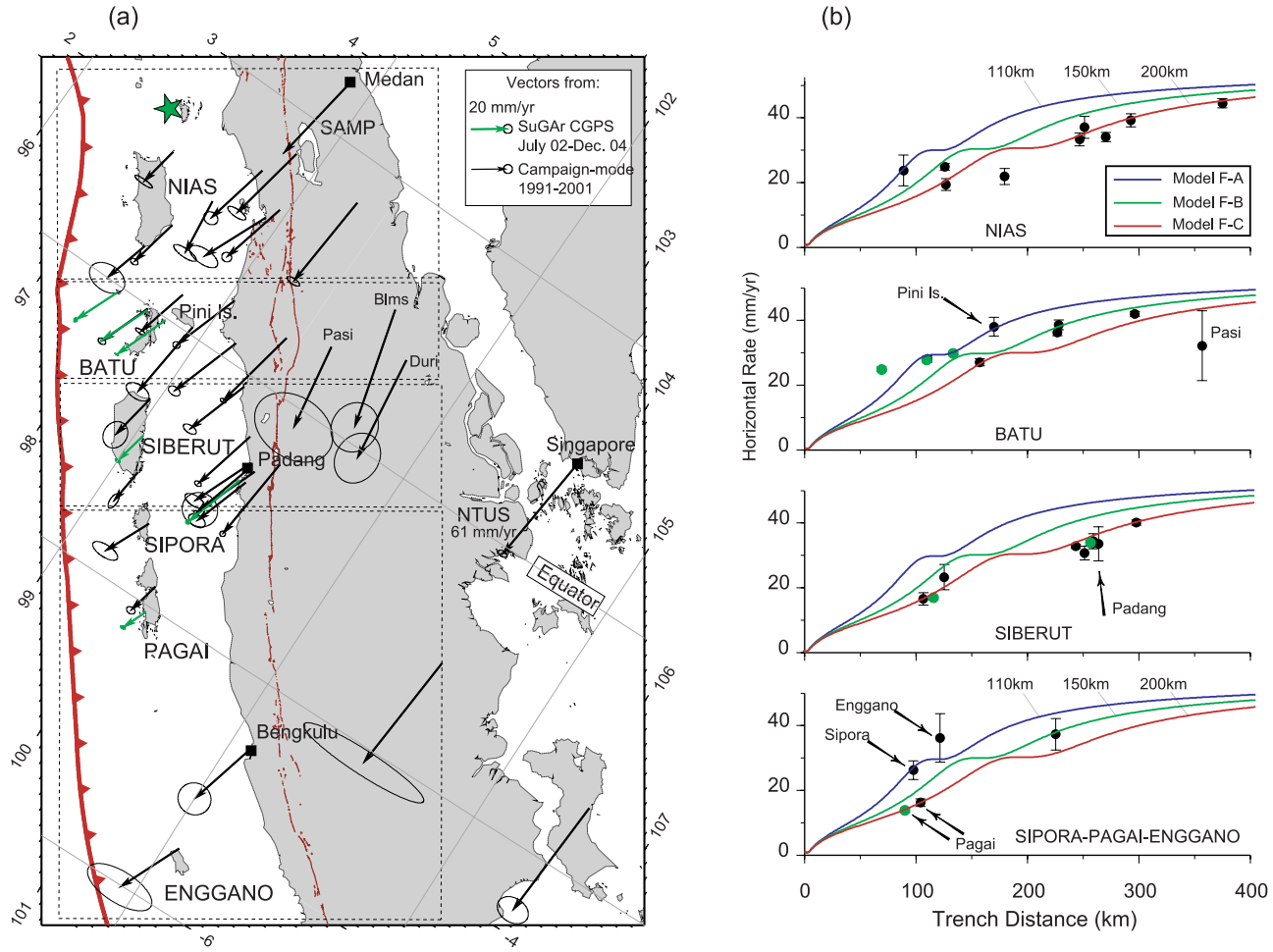

Figure 5. Horizontal velocities relative to Australia (a) in map view and (b) along sections normal to the trench. Black arrows represent velocities determined from GPS campaign measurements [*Bock et al.*, 2003], and green arrows show velocities determined from continuous GPS measurements at stations of the Sumatra Geodetic Array, SuGAr (http://sopac.ucsd.edu/cgi-bin/sugarTimeSeries.cgi), prior to the occurrence of the Sumatra-Andaman earthquake of 2004. Ellipses show 1σ uncertainties (Tables 3 and 4). Boxes in Figure 5a show location of swath used to construct profiles in Figure 5b. Except at Enggano and Sipora, horizontal velocities decrease noticeably trenchward, as expected if the shallower portion of the megathrust is locked. The large velocities at Enggano and Sipora suggest little locking around these stations. Continuous lines show velocity profiles predicted from forward models F-a, F-b, and F-c (Table 5). These models assume full locking of the megathrust from the trench to a horizontal distance of 110, 150, and 200 km, respectively.

data, provided exclusion of the stations showing an obvious postseismic response to the 2004 and 2005 ruptures.

[25] In order to isolate the pattern of interseismic strain associated only with the megathrust, we correct for the effect of interseismic strain along the Sumatran fault. We build an interseismic model for the Sumatran fault using locking depths on the fault of 10–20 km as estimated by *Genrich et al.* [2000] and *Prawirodirdjo et al.* [2000]. This model predicts displacements no greater than 1 to 4 mm/a for GPS points located on the Sumatran coast and less than 0.5 mm/a on the islands, and negligible vertical rates at the paleogeodetic sites.

[26] Having subtracted the effect of interseismic motion on the Sumatran fault, the residual velocity vectors can be ascribed to interseismic strain associated with the megathrust. To model this, we adopt the back-slip modeling approach [*Savage*, 1983], in which only the portion of the plate interface that is partially or fully locked needs to be considered. The surface deformation field caused by distributed creep along the megathrust is computed using the theory of dislocations in an elastic half-space [*Okada*, 1992]. The slip vector on the megathrust is assumed to remain parallel to the long-term interplate velocity (Figure 2), and the interseismic coupling is constrained to range between 0 (decoupled) and 1 (fully coupled).

[27] We quantify the misfit between the observations and any model predictions using a reduced chi-square criterion defined here as:

$$\chi_r^2 = 1/n \sum_{i=1,n} ((obs_i - pred_i)/\sigma_i)^2 \qquad (1)$$

Table 2. Original Vertical Velocitiy Vu and the Assigned 1σ Uncertainty σ_{Vu} for the Period 1962–2000[a]

Longitude °E	Latitude °N	Vu, mm/a	σ_{Vu}, mm/a	Location	Period	D, km
98.34517	−0.50046	−4.0	0.9	Bendera	1950–2000	86
98.46383	−0.53921	−7.1	1.6	Badgugu-A	1952–1997	94
98.47135	−0.54982	−6.4	3.0	Badgugu-B	1945–1998	94
98.41148	−0.30814	−3.7	0.4	Barogang	1950–1997	105
98.29730	−0.1021	−0.3	1.4	Pono	1970–1985	108
98.32066	−0.05011	−1.1	0.3	Antinang	1950–1997	113
98.52170	−0.38391	−0.8	0.3	Tofa	1950–1997	109
98.29770	0.053	0.3	0.5	Memong	1966–1997	118
98.57430	−0.28378	3.6	2.0	Tj. Anjing	1985–1997	121
98.52300	−0.1486	3.1	1.2	Penang	1975–1997	125
98.46046	0.03942	2.4	0.9	Lago	1969–1997	132
98.54380	−0.0739	2.9	4.0	Bais	1958–1997	132
98.62361	0.08225	−0.9	0.5	Masin	1950–1991	149
98.60184	0.18609	1.2	0.8	Lambak	1971–1996	154
98.93160	0.048	2.2	0.9	Sambulaling	1970–1996	174
99.35970	0.1286	−0.4	1.7	Telur	1983–1997	218
98.91245	−0.94161	−2.2	0.8	L. Bajau	1972–1997	125
98.94749	−1.04308	−3.7	0.8	TabekatA	1946–1995	121
98.94708	−1.0396	−7.5	1.3	TabekatC	1955–2001	122
99.07342	−1.2687	−4.1	1.4	TelukSaibi	1951–1997	118
99.11329	−1.37063	−6.5	1.0	Saibi	1956–1989	114
99.20546	−1.56169	−4.3	2.7	Malepet	1983–1997	110
99.28944	−1.63937	−6.3	0.7	Mapinang	1951–1998	112
99.29230	−1.73737	−7.4	0.3	Beuasak	1946–1998	106
99.26492	−1.77189	−9.5	1.6	Libut	1960–1997	101
99.29427	−1.82509	−14.3	3.3	Masokut	1969–1997	100
100.09770	−0.6332	−1.8	0.9	Angsa	1965–1997	251
99.59751	−1.994576352	−8.5	0.7	P. Panjang	1934–1985	110
99.59202	−2.03311144	−10.7	1.5	Tuapejit	1968–1998	107
99.80205	−2.289429173	−4.4	1.2	Sikici	1951–2002	109
99.53567	−2.13171068	−5.8	1.5	Pitogat	1962–1985	96
99.74060	−2.37033039	−8.3	1.6	Siruamata	1957–1995	98
99.99514	−2.7520595	−9.7	2.5	Silabu	1986–2000	95
100.10150	−2.59419078	−8.3	1.2	Simanganya-A	1962–1995	115
100.28281	−2.825880981	−7.1	1.7	Singingi	1958–2003	116
100.31110	−3.127471786	−13.4	1.3	Bulasat	1955–2002	99
100.46251	−3.037994043	−6.0	2.6	Sibelua	1956–2002	118
100.44658	−3.285214886	−7.1	2.4	Bangkaulu	1962–2003	100
100.15215	−2.852633	−8.8	2.1	Siruso	1965–1995	103
100.50499	−3.16275	−4.1	0.8	Taitanopo	1969–1995	113
100.48669	−3.215888	−5.2	1.8	Siatanusa	1954–1995	108
100.67938	−3.4545	−9.5	2.0	Stupai	1949–1995	109
100.67683	−3.4805	−9.6	1.7	Sanding-A	1942–1996	107
102.2100	−3.82	−2.0	0.6	Tikos	1966–1996	220

[a]From *Natawidjaja et al.* [2004, 2007]. No eustatic correction is applied.

where n is the number of observations and σ_i the uncertainty assigned to the ith datum. Note that this criterion differs from the standard reduced chi-square criterion, in which n should be replaced by n-p, p being the number of free parameters involved in the modeling. Since the cost function induces some correlation between the model parameters that varies with the weights put on the smoothness and the rate of accumulation of moment deficit, the number of free parameters used in the formal inversion models presented below is hard to define. We decide then to not take p into account in the chi-square computation. If a model adjusts the data with errors of the order of the uncertainties assigned to the observations, then χ^2_r should be of the order of 1. Given that it is not obvious that the uncertainties assigned to the geodetic and paleogeodetic data are really comparable and representative of the 67% confidence domain, we compute the reduced chi-square considering the various types of data (paleogeodesy, campaign mode GPS, CGPS) separately before combining them. Normalization would have required multiplication of the uncertainties on the velocities determined from the CGPS stations by a factor of 4 for the horizontal components, and a factor of 7 for the vertical component. The uncertainties on the coral data would have been multiplied by a factor of 2 and those on the GPS campaign mode data by a factor 2.5. This indicates that the uncertainties on the CGPS data might be significantly underestimated compared to those on the other type of data. This is probably because the uncertainty on the correction of seasonal variations (mostly due to mismodeling of tropospheric effect) is ignored although it could be significant given the short time period covered by the CGPS data. The difference between solutions obtained from the inversion of all the data with or without normalization of uncertainties was found to be insignificant. Therefore, we decided not to normalize the uncertainties in the joint inversions presented here.

[28] For reference we have estimated the misfits of the forward models described above (Figures 4b and 5b) in which the plate interface is locked over a constant width of

Table 3. GPS Velocities in the ITRF2000 Reference Frame for the Period 1991–2001[a]

Longitude °E	Latitude °N	Ve, mm/a	Vn, mm/a	σ_{Ve}, mm/a	σ_{Vn}, mm/a	Site	Period
99.38	0.22	24.9	11.8	1.4	0.9	Airb	1991–2001
99.76	−0.15	26.6	16.5	1.6	0.8	Ajun	1991–2001
98.17	1.46	40.6	19.8	2.9	0.9	Bint	1991–2001
100.75	1.65	54.2	−11.6	4.9	5.5	Blms	1991–1993
99.27	−1.73	36.3	31.4	0.8	1.8	D937	1991–2001
98.52	0.34	30.2	21.8	1.3	0.4	D944	1991–2001
98.84	0.08	33.0	6.2	2.8	1.5	D947	1991–2001
98.27	−0.03	27.5	22.5	0.9	0.6	D949	1991–2001
97.81	0.55	30.6	25.2	4.2	2.8	D952	1991–2001
97.94	0.95	31.7	22.9	0.9	0.6	D953	1991–2001
97.44	1.68	33.1	28.1	2.3	0.5	D962	1991–2001
99.62	2.46	32.6	−2.1	1.6	0.6	Demu	1991–2001
101.21	1.22	44.8	−5.5	4.6	5.7	Duri	1991–1993
102.16	−5.25	24.3	18.3	7.9	3.4	Engg	1992–1994
103.64	−1.62	32.4	−13.7	15.3	2.6	Jamb	1992–1994
98.45	2.12	28.8	14.3	1.6	1.3	Julu	1991–2001
100.65	−0.70	33.3	4.5	0.6	0.6	Kaca	1991–2001
102.25	−3.75	28.4	13.4	3.6	3.4	Kulu	1992–1994
98.68	2.52	28.6	7.0	2.3	0.8	Mart	1991–2001
98.90	−0.91	33.5	24.7	2.5	3.0	Nsib	1991–2001
100.42	−1.10	28.0	20.3	2.0	1.2	P003	1993–2001
99.85	0.62	28.4	5.0	0.7	0.4	P37e	1991–2001
100.36	−0.94	28.0	16.3	0.6	0.5	Pada	1991–2001
100.35	−0.87	24.5	18.3	2.4	1.1	Padu	1996–2001
100.21	−2.75	34.9	33.7	1.0	0.7	Paga	1992–2001
98.81	1.67	21.8	15.2	3.5	1.6	Pand	1991–2001
100.36	0.83	44.8	5.1	9.1	6.6	Pasi	1991–1993
98.90	1.85	28.0	14.3	1.1	1.0	Pisa	1991–2001
99.08	0.63	25.3	14.1	0.8	0.7	Sika	1991–2001
99.73	−2.17	27.4	26.4	3.1	1.3	Siob	1996–2001
100.44	−0.94	25.2	18.8	3.9	3.6	Spg2	1991–2001
100.16	−0.62	29.1	15.5	0.8	0.5	Tobo	1991–2001
106.14	−2.14	33.6	−13.1	3.6	2.6	Kalp	1992–1994
103.68	1.34	30.8	−8.6	1.1	0.6	NTUS	1991–2001

[a]From *Bock et al.* [2003]. The displacements recorded by the International GNSS Service (IGS) station at Singapore (NTUS) were integrated in this analysis.

Table 4. Unfiltered Solution of the Permanent SuGAr (Sumatran GPS Array) GPS in the ITRF2000 Reference Frame[a]

Longitude, °E	Latitude, °N	Ve, mm/a	Vn, mm/a	σ_{Ve}, mm/a	σ_{Vn}, mm/a	Site	Period	Vu, mm/a	σu, mm/a
100.28	−3.07	34.51	38.71	0.97	0.56	BSAT	02.7–04.9		
99.08	−1.32	34.91	32.78	0.83	0.55	MSAI	02.6–04.9		
98.52	−0.03	27.53	21.82	0.74	0.55	PBAI	02.6–04.9		
100.35	−1.12	28.59	19.20	0.98	0.61	PSKI	02.6–04.9		
97.86	−0.08	29.33	26.42	0.42	0.80	PSMK	02.6–04.2		
98.28	−0.05	27.70	24.12	0.31	0.49	PTLO	02.6–04.8		
98.71	3.62	28.70	−0.43	0.10	0.10	SAMP	02.6–04.9		
99.38	0.220	16.93	9.63	0.50	0.60	ABGS	Jun 2005/Oct 2006		
100.28	−3.07	36.37	39.85	0.60	0.30	BSAT	Jun 2005/Oct 2006	−14	0.7
98.64	−1.28	40.86	37.12	1.40	0.50	BTET	Aug 2005/Oct 2006	−22.7	2.1
103.52	−1.61	27.20	−0.91	0.50	0.20	JMBI	Jun 2005/Oct 2006		
101.70	−3.30	1.87	22.11	2.20	0.70	LAIS	Jan 2006/Oct 2006	−26.2	3.7
101.15	−2.28	28.67	18.66	0.50	0.60	LNNG	Jun 2005/Oct 2006	−17.1	3.6
99.08	−1.32	39.33	29.58	0.80	0.49	MSAI	Jun 2005/Oct 2006	−7.4	1.3
101.09	−2.54	30.64	21.03	0.40	0.50	MKMK	Jun 2005/Oct 2006	−18.7	3.2
102.27	−5.35	8.80	9.88	1.10	0.40	MLKN	Aug 2005/Oct 2006	−22.7	1.6
102.89	−4.45	−0.70	12.28	2.10	0.70	MNNA	Jan 2006/Oct 2006	−23.9	3.3
99.26	−1.79	41.08	36.99	1.20	0.70	NGNG	Jun 2005/Oct 2006	−20.6	1.3
98.51	−0.63	31.50	19.15	3.80	0.30	PBJO	Aug 2005/Oct 2006	−20.2	1.5
99.60	−1.99	28.39	35.13	3.90	0.40	PPNJ	Jun 2005/Oct 2006	−24.0	1.9
100.39	−2.96	34.27	32.15	0.50	0.20	PRKB	Jun 2005/Oct 2006	−24.4	2.0
100.35	−1.12	26.19	17.53	0.50	0.46	PSKI	Jun 2005/Oct 2006	−7.8	1.6
100.00	−2.76	34.18	37.41	0.50	0.20	SLBU	Jun 2005/Oct 2006	−25.7	1.8
103.68	1.34	28.53	−5.92	0.07	0.05	NTUS	Jun 2005/Oct 2006		

[a]The first GPS monuments were installed during the summer 2002. In the upper block, velocities were computed until the occurrence of 26 December 2004 Sumatra-Andaman earthquake. In the lower block, GPS velocities from June 2005 or later if the GPS station was installed afterward to October 2006. Vu and σu are the vertical velocities and associated uncertainties when available.

Table 5. Reduced χ^2_r Computed for a Variety of Forward Models[a]

Name	U_{LFZ}, km	D_{LFZ}, km	χ^2_r All Data	χ^2_r Coral Data	χ^2_r GPS Data	$\dot{M}_o$, 10^{20} N m/a
F-a	6	30	120.1	218.0	22.3	5.33
F-b	6	40	26.3	27.4	25.3	7.05
F-c	6	50	38.8	31.4	46.3	8.75
F-d	6	30–55	22.6	26.7	18.6	6.88
F-e	15	30–55	17.7	22.1	13.4	4.17
F-f	6–25	30–55	16.6/8.6[b]	24.2/9.1[b]	9.07/8.2[b]	6.09

[a]The accumulation rate of seismic moment deficit $\dot{M}_o$ is computed by assuming an average shear modulus of 64 GPa. This value was chosen for consistency with the Earth model used in the modeling of the seismic sources and in the formal inversions. The updip limit of the locked fault zone, U_{LFZ}, is along the trench (at a depth of 6 km) or deeper and the depth of the downdip limit, D_{LFZ}, is varied from 35 to 55 km. For all these models, the coupling is either 1 (fully locked) or 0 (fully creeping).

[b]Misfit computed without the measurements from Pini island (two corals at Lambak and Masin, Figure 4, and one GPS point, Figure 5).

either 110, 150 or 200 km (models F-a, F-b and F-c in Table 5). The χ^2_r for the coral data considered alone is about 218 if the width of the locked fault zone is 110 km, 27 if its width is 150 km, and 31 if its width is 200 km. When all the GPS data are considered, the χ^2_r is about 22 for a width of 110 km, is about 25 for a width of 150 km and increases to 46 for a locked fault zone width of 200 km. From these laterally homogeneous locked fault zone models, the fit to the geodetic and paleogeodetic data is best for an average locked fault zone width of 150 km, which corresponds to an average depth of 40 km. For each model, we estimate the rate of accumulation of slip potency deficit, defined as the integral of slip rate deficit over the locked fault zone surface. That potency rate multiplied by the shear modulus equals the moment deficit accumulation rate, $\dot{M}_o$, for the whole study area between 2°N and 6°S (Table 5).

[29] It is not possible to obtain a satisfying fit to the data if it is assumed that the locked fault zone is fully locked and has a constant width. The data suggest significant lateral variations with relatively less coupling beneath the Batu and Enggano islands than beneath the Mentawai islands. Thus we now test models with lateral variations of coupling in which the downdip end (D_{LFZ}) and of the updip end (U_{LFZ}) of the locked fault zone vary, but the locked patch is fully coupled between these limits ($v/v_0 = 1$). In the manner described in section 4.2, we place upper bounds on coupling by maximizing the width of the locked fault zone where the data place some constraints on U_{LFZ} and D_{LFZ}. In between those locations, the geometry of the locked fault zone is assumed to vary linearly. Formally, the sparseness of data allows more complex lateral variations in the width of the locked fault zone. In particular it could be much wider than what we allow wherever the data coverage is poor. Nonetheless, we seek the simplest model that fits the data by assuming smooth and monotonic variations of the locked fault zone's downdip and updip edges.

[30] In section 4.3 we present formal inversions in which the rate of moment deficit accumulation, $\dot{M}_o$, is varied, and use that approach to determine the minimum value of $\dot{M}_o$ needed to fit the geodetic and paleogeodetic data. These two approaches explore two different ways of introducing lateral variations in interseismic coupling. The first (forward modeling) introduces fewer free parameters than the second (inverse modeling). Together, they constrain the range of possible values in the rate of moment deficit accumulation, $\dot{M}_o$.

4.2. Forward Modeling of the Pre-2004 Paleogeodetic and Geodetic Data

[31] We have first tested simple forward models of interseismic strain, which were adjusted by trial and error. In these cases, the megathrust is either fully locked or creeping at the secular slip rate, meaning the coefficient of coupling is either 0 or 1. The megathrust interface is meshed with about 100 triangular elements. A source point exists at the centroid of each element to simulate the dislocation. The estimation of the surface deformation with that geometry is computed in an elastic half-space dislocation algorithm [*Okada*, 1992]. To compare the corresponding rate of accumulating moment deficit we use an averaged shear modulus of 64 GPa, which corresponds to the average of the one-dimensional (1-D) CRUST2.0 layered structure model in the seismogenic depth range 0–50 km (Table 6) [*Bassin et al.*, 2000].

[32] Given this megathrust geometry and the fault slip direction imposed by the secular motion of fore-arc sliver relative to Australia, interseismic strain depends exclusively on the coupling distribution of the locked fault zone. We first assume a locked fault zone extending all the way to the trench and adjust the downdip limit. In this case, the best possible fit corresponds to the forward model F-d in which the downdip limit of the locked fault zone varies between 35 and 55 km depth (Table 5 and Figure 6a). The χ^2_r of model F-d is 22 if all data are considered. It is 26 if the coral data are considered alone and 18 for the GPS data. This model systematically overestimates subsidence rates or underestimates horizontal velocities at a number of sites nearest the trench. These deficiencies imply that a model with some decoupling along the shallower portion of the megathrust would fit the data better.

[33] We first examine the effect of decoupling the shallowest parts of the megathrust by calculating a model in which the updip limit of the locked fault zone is 15 km deep everywhere (model F-e, Table 5 and Figure 6b). The effect of this shallow decoupling is to increase the GPS velocities of sites on the Mentawai islands relative to the Australian plate, without increasing the misfit to the vertical data and to the GPS sites on the Sumatran mainland. In particular, the GPS vectors from sites on

Table 6. CRUST2.0 Structure From *Bassin et al.* [2000] Used in the Inversion of Geodetic and Paleogeodetic Data

Thickness, km	Vs, km/s	Vp, km/s	ρ, kg/m^3	$\mu = \rho(\mathrm{Vs})^2$, GPa
1.7	2.500	5.000	2.6000	16.25
2.3	3.650	6.600	2.9000	38.63
2.5	3.900	7.100	3.0500	46.39
196	4.473	8.080	3.3754	67.53
36	4.657	8.594	3.4465	74.60
108	4.707	4.707	3.4895	77.31

the southern coast of Nias island, on the Batu islands, on Sipora and Enggano islands are much better reproduced by model F-e (Figure 6b).

[34] To improve the fit further and yet keep the extent of the locked fault zone as large as possible, we now vary the updip limit of the locked fault zone (model F-f in Table 5 and Figure 6c) so that wherever the data allow it, the locked fault zone extends all the way to the trench. Also, we assume that the downdip end of the locked fault zone extends as deep as possible between Pagai island and Enggano, where the data are sparse. The χ^2_r of model F-f is less than 10 for the GPS data alone and about 24

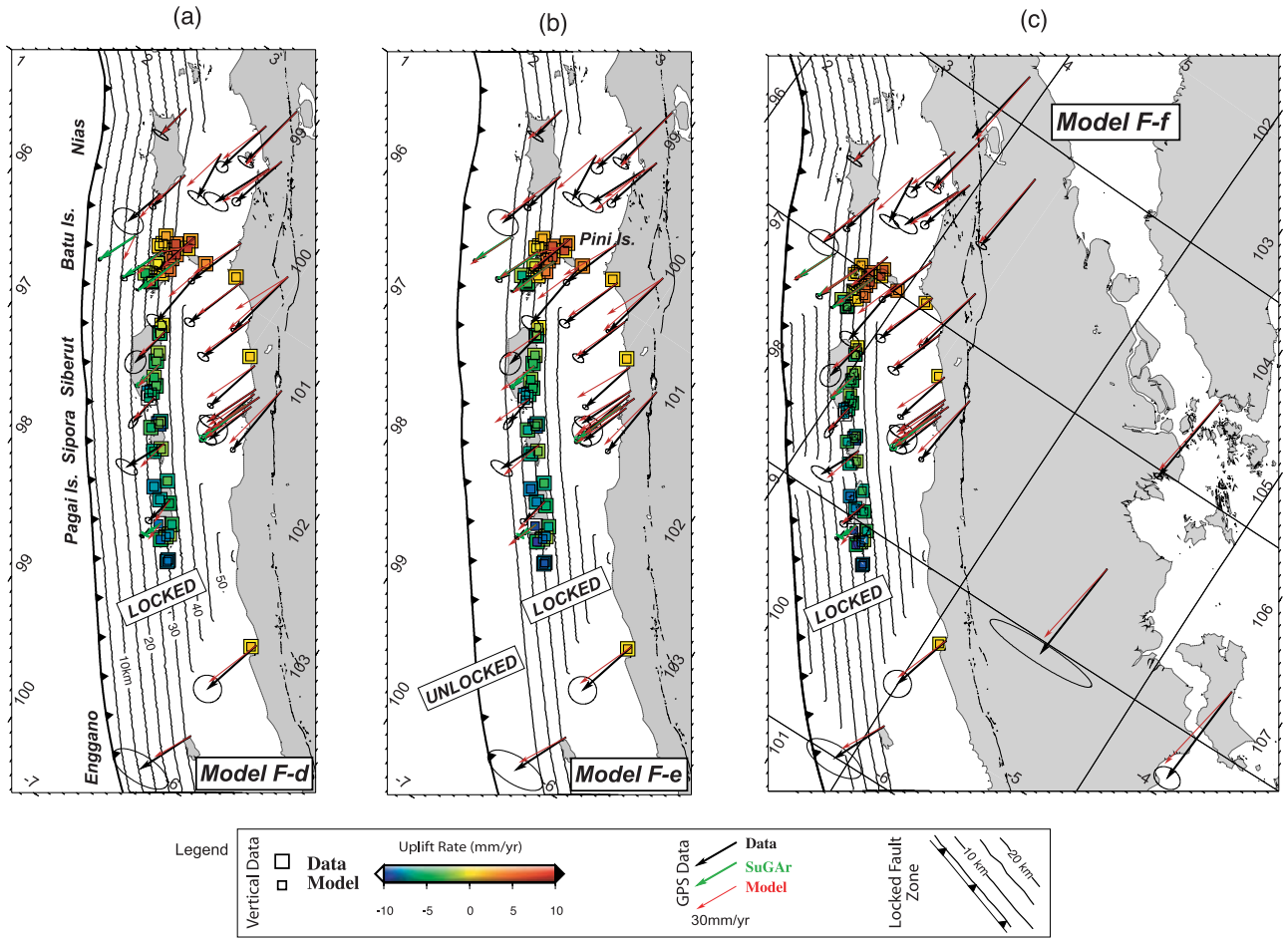

Figure 6. Comparison of observed and predicted velocities (red vectors) computed from three reference models with variable locked fault zone width (forward models F-d, F-e, and F-f). Contour lines on the megathrust (5-km depth intervals) indicate the portion of the megathrust that is assumed fully locked. Velocities derived from campaign GPS measurements and from continuous GPS measurements at the SuGAr stations are shown in black and green, respectively. Predicted (small squares) and measured (larger squares) vertical rates are color coded. The color difference between the inner and outer squares reflects of the fit of model to data. Table 5 lists all these models with their respective χ^2_r values. (a) Model F-d. The locked fault zone extends from the trench to a variable depth that was adjusted by trial and error. The misfits between the observed and predicted velocities in the Batu and Sipora islands in particular show that varying the location of the updip edge of the locked fault zone would improve the fit. (b) Model F-e. The updip limit of the locked fault zone is everywhere 50 km away from the trench. The data from the Batu and Sipora islands are better fit than in model F-d but at the cost of a poorer fit to many other data points. (c) Model F-f. The updip limit of the locked fault zone varies laterally. Three regions of shallow interseismic slip are introduced trenchward of the Batu, Sipora, and Enggano islands.

for the coral data. Coral and GPS measurements near Pini island, the eastern island of the Batu archipelago, contribute greatly to the high misfits. *Natawidjaja et al.* [2004] noted that the coral sites of Masin and Lambak, on or near Pini island, are inconsistent with the surrounding pattern of deformation (compare Figure 4) and suggested that this indicates deformation associated with secondary structures above the megathrust. This interpretation is supported by an anomalous horizontal velocity at the GPS site on the southern east side of Pini island (Figure 5a). If we exclude the data from Pini island, the reduced χ^2 drops to 9.1 for the coral data and 8.2 for the GPS measurements.

[35] Forward model F-f provides a reasonable fit to the geodetic and paleogeodetic data. It represents an upper bound on the amount of coupling along the megathrust and implies a rate of accumulation of moment deficit, $\dot{M}_o$, of 6.09 10^{20} N m/a between 2°N and 6°S. Two narrow locked patches beneath the Batu islands and Enggano bound a 600-km-long patch that is locked to the trench (Figure 6c). A thin patch of shallow decoupling bisects this long coupled patch near Sipora island at about 3°S.

[36] The models discussed in this section provide a much better fit to the data than the simple models F-a, F-b, and F-c, which have no lateral variation of coupling. An even better fit to the data could be achieved by allowing the degree of interseismic coupling within the locked fault zone to be heterogeneous. This is one option we explore in the inverse models of section 4.3.

4.3. Formal Inversions of the Pre-2004 Paleogeodetic and Geodetic Data

[37] In this section, we determine the best fitting heterogeneous distribution of coupling along the plate interface from a formal inversion of the geodetic and paleogeodetic data with the constraint that the rate of accumulation of moment deficit, $\dot{M}_o$, be as close as possible to some a priori value, $\dot{M}_o'$. We adopt the inversion procedure of *Ji et al.* [2002], used previously to invert for the coseismic slip distribution of the Sumatra-Andaman and Nias-Simeulue earthquakes [*Chlieh et al.*, 2007; *Konca et al.*, 2007; *Subarya et al.*, 2006] assuming the 1-D CRUST2.0 layered structure (Table 6). The megathrust consists of 670 rectangular 20 km × 20 km dislocation surfaces. The two parameters associated with each dislocation element are its rake and coefficient of coupling. The slip azimuth cannot deviate more than 20° from that predicted by the secular motion of the fore-arc sliver relative to Australia, and the coefficient of coupling is able to vary between 0 and 1.

[38] The cost function consists of the summation of the weighted sum-of-residuals squared (each datum is weighted in proportion to its 1σ uncertainty), $\chi^2 = \sum_{i=1,n} ((\mathrm{obs}_i - \mathrm{pred}_i)/\sigma_i))^2$, and two other terms meant to control the smoothness and the accumulation rate of moment deficit:

$$\mathrm{Cost} = \chi^2 + \lambda_1(\Delta c/\alpha)^2 + \lambda_2\left(\left(\dot{M}_o - \dot{M}_o'\right)/\beta\right)^2 \qquad (2)$$

where Δc is the average difference of coupling between adjacent cells, $\dot{M}_o'$ is an a priori scalar moment rate. The coefficient λ_1 controls the smoothness of the solution and λ_2 modulates the weight assigned to minimize the total moment. The normalization coefficients α and β are determined so that for $\lambda_1 = \lambda_2 = 1$, the three criteria have equal importance, meaning that for the best fitting model $\chi^2 = (\Delta c/\alpha)^2 = ((\dot{M}_o - \dot{M}_o')/\beta)^2 = \mathrm{Cost}/3$. Resolution tests described in Appendix B show that the data coverage provides reasonable constraints on the distribution of coupling along the plate interface between 2°N and 6°S.

Table 7. Reduced χ_r^2 and Moment Deficit Accumulation Rate $\dot{M}_o$ Obtained From the Inversion of the Paleogeodetic and Geodetic Data Collected Before the Occurrence of the 2004 Sumatra-Andaman Earthquake[a]

Inversion Models	$\dot{M}_o$, 10^{20} N m/a	χ_r^2		
		All Data	Coral Data	GPS
I-a	4.0	3.9	4.1	3.7
I-b	3.0	5.2	5.7	4.7
I-c	2.0	9.8	8.2	11.4
I-d	4.5	3.8	4.1	3.5
I-e	5.5	3.7	4.0	3.4
I-f	6.7	3.6	3.9	3.3
I-g	7.6	3.7	4.0	3.4
I-h	8.0	3.9	4.1	3.7
I-I	9.2	5.6	6.2	5.0

[a]The coupling is allowed to vary smoothly in the range [0, 1]; χ_r^2 is minimum when no constraints are applied on the accumulated seismic moment. The misfit to the data increases when the accumulated seismic moment is forced to be lower than 4×10^{20} N m (models I-b and I-c).

[39] We have run several inversions of the whole data set in which we have put a strong constraint on the moment deficit accumulation rate ($\lambda_2 > 10$) and varied the a priori value from 2×10^{20} N m/a to 9×10^{20} N m/a (Table 7 and Figure 7). This suite of models shows that the misfit starts to degrade when $\dot{M}_o$ decreases to about 4×10^{20} N m/a. The fit to the data does not degrade much as $\dot{M}_o$ increases (Figure 7). This reflects the fact that the sparseness of the data allows the locked fault zone to extend downdip from the trench to the 200-km spatial limit of the model. Because they exhibit locking to great depths, we consider the models corresponding to $\dot{M}_o'$ in excess of about $6-7 \times 10^{20}$ N m/a unrealistic.

[40] Model I-a, which corresponds to 4×10^{20} N m/a, is representative of the minimum coupling along the plate interface required to fit the data. The distribution of coupling in this model appears in Figure 8 and has a χ_r^2 of 3.9. For comparison, if the accumulated moment rate $\dot{M}_o$ is reduced by one fourth, (3×10^{20} N m/a), χ_r^2 increases to 5.2 (model I-b, Table 7). If $\dot{M}_o$ is 2×10^{20} N m/a, χ_r^2 jumps to 9.8 (model I-c, Table 7). These three models yield similar distributions of coupling, with more peaked asperities in the model with the lowest rate of accumulation of moment deficit.

4.4. Four Interseismic Coupling Determined From the 2005–2006 SuGAr Data

[41] We now perform a similar analysis that utilizes the secular velocities determined from SuGAr data collected after the 2004–2005 earthquakes (Table 4). This gives us better spatial coverage than the preearthquake SuGAr data, because several stations began recording after or just shortly before the two earthquakes. We exclude data from stations near and north of the equator though, because postseismic transients close to the source of the 2005

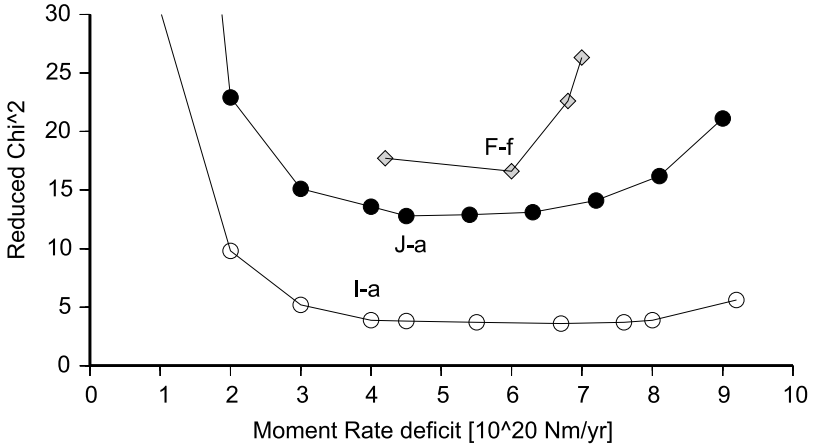

Figure 7. Variation of reduced χ_r^2 as function of the seismic moment rate deficit, $\dot{M}_o$, for a variety of models obtained by forward modeling (gray diamonds, Table 5), formal inversion of the geodetic and paleogeodetic data prior to the 2004 Sumatra-Andaman earthquake (white circles, Table 7), and formal inversion of the whole data set including the SuGAr GPS data posterior to the 2005 Nias-Simeulue earthquake (black circles, Table 8). These models bound the accumulated seismic moment rate for the area between Nias and Enggano islands (i.e., between 2°N and 6°S,) to between 4×10^{20} N m/a and 6×10^{20} N m/a.

earthquake obscure the secular signal. Although the period covered is short, the velocities are sufficiently well constrained to yield a first-order estimate of the pattern of geodetic strain over that area.

[42] In this second suite of inversions, we have followed the same procedure as in the formal inversion of the pre-2004 geodetic data. The best fitting model (Table 8 and Figure 9) exhibits strong coupling beneath Siberut, Sipora and the Pagai islands and an abrupt transition to very little coupling to the south. The pattern is remarkably similar to the pattern inferred from the pre-2004 geodetic and paleogeodetic data (Figure 8), even though the two SuGAr data sets are independent and behavior south of the Pagai islands is only poorly constrained by the pre-2004 data. The main difference between the two models is a trough of low coupling just east of Siberut and Sipora islands in the inversion of the pre-2004 data set. This trough might in part be the result of the amount of weight put on minimizing the moment, or it might reveal a temporal change. Regardless, each of the two models indicate that coupling is strong beneath the Mentawai islands and that farther south the megathrust has a strong aseismic component of interseismic slip.

4.5. Five Joint Inversions of the Pre-2004 and Post-2005 Data

[43] Because the preearthquake and postearthquake data sets yielded quite similar distributions of coupling when considered independently, we can justify performing an inversion that uses the pre-2004 paleogeodetic and geodetic data and the 2005–2006 SuGAr data together. This yields significant improvement in resolution, because the complete data set has better spatial resolution. However, the quality of the fit is degraded because velocities obtained from campaign GPS monuments and from nearby SuGAr CGPS stations differed in some cases. The best fitting model J-a (Figure 10) has a χ_r^2 of 12.8 (Table 8 and Figure 7) and corresponds to a moment deficit accumulation rate of 4.5×10^{20} N m/a. The relatively high χ_r^2, is probably due in part to underestimation of uncertainties assigned to the SuGAr GPS measurements and in part to temporal variation of coupling. Tests show that varying the weighting of the SuGAr data relative to the coral data does not significantly alter the distribution of coupling derived from this joint inversion. Hence, we consider that model J-a is a reasonable best estimate of the distribution of interseismic coupling on the megathrust.

5. Discussion

5.1. Comparison of Interseismic and Seismic Coupling Between 2°N and 6°S

[44] The Sumatran geodetic and paleogeodetic data are consistent with the prevailing view that locking occurs at shallow depths and aseismic slip occurs at depths greater than about 40 km. Through the past half century, moment deficit has been accumulating on the megathrust between latitudes 2°N and 6°S at a rate between 4.0×10^{20} N m/a (model I-a, Figure 8) and 6.0×10^{20} N m/a (model F-f, Figure 6c). This is roughly equivalent of storing, over this 800-km-long stretch of the megathrust, the moment of a M_w 8.7 earthquake every 20 years.

[45] Figure 11 illustrates a comparison of accumulated interseismic moment deficit and accumulated seismic moment for the past three centuries between latitudes 2°N and 6°S. In constructing Figure 11, we assume that the spatial pattern of interseismic coupling has been stationary and that the rates of accumulation of moment deficit have not varied with time. Models I-a and F-f, then, provide lower and upper bounds on the rate of accumulating deficit. For reference, we also show model F-b, which represents the accumulated deficit if one assumes full locking to 40 km, a depth commonly used to estimate seismic coupling [e.g., *Tichelaar and Ruff*, 1993].

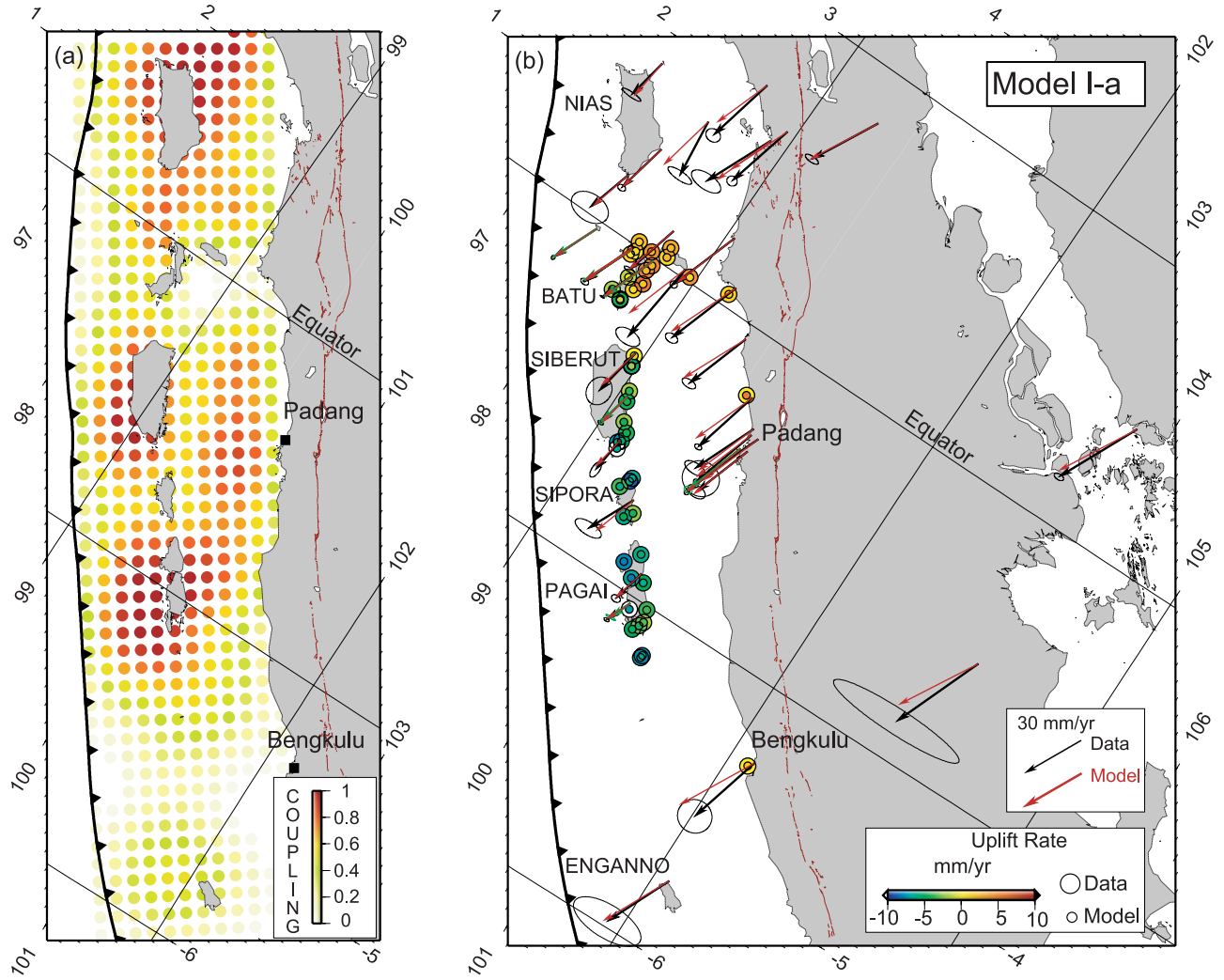

Figure 8. Distribution of coupling on the Sumatra megathrust derived from the formal inversion of the coral and of the GPS data (Tables 2, 3, and 4) prior to the 2004 Sumatra-Andaman earthquake (model I-a in Table 7). (a) Distribution of coupling on the megathrust. Fully coupled areas are red, and fully creeping areas are white. Three strongly coupled patches are revealed beneath Nias island, Siberut island, and Pagai island. The annual moment deficit rate corresponding to that model is 4.0×10^{20} N m/a. (b) Observed (black vectors) and predicted (red vectors) horizontal velocities appear. Observed and predicted vertical displacements are shown by color-coded large and small circles, respectively. The χ^2_r of this model is 3.9 (Table 7).

Table 8. Reduced χ^2_r and Moment Deficit Accumulation Rate $\dot{M}_o$ Obtained From the Inversion Models of All the Paleogeodetic and Geodetic Data Before and After the 2004 and 2005 Sequence[a]

Inversion Models	$\dot{M}_o$, 10^{20} N m/a	χ^2_r				
		All Data	Coral Data	GPS Before 26 Dec 2004	GPS After 26 Dec 2004	Vertical After 26 Dec 2004
J-a	4.5	12.8	4.5	6.2	17.4	58.9
J-b	3.0	15.1	4.3	8.7	21.4	64.2
J-c	2.0	22.9	3.9	22.0	29.9	69.0
J-d	4.0	13.0	4.5	6.5	17.2	60.6
J-e	5.4	12.9	4.5	6.2	17.2	60.3
J-f	6.3	13.1	5.1	6.1	18.7	57.3
J-g	7.2	14.1	5.5	6.2	23.1	56.2
J-h	8.1	16.2	6.1	6.6	32.3	54.6
J-i	9.0	21.1	6.7	9.1	49.5	54.5
SuGAr alone	4.5	24.5			14.8	48.0

[a]The misfit to the data increases when the accumulated seismic moment is forced to be lower than 4×10^{20} N m (models J-b and J-c) or higher than 7×10^{20} N m (models J-g, J-h, and J-i). SuGAr alone data are the result from the inversion of the velocities measured between June 2005 and October 2006 at the SuGAr CGPS stations alone.

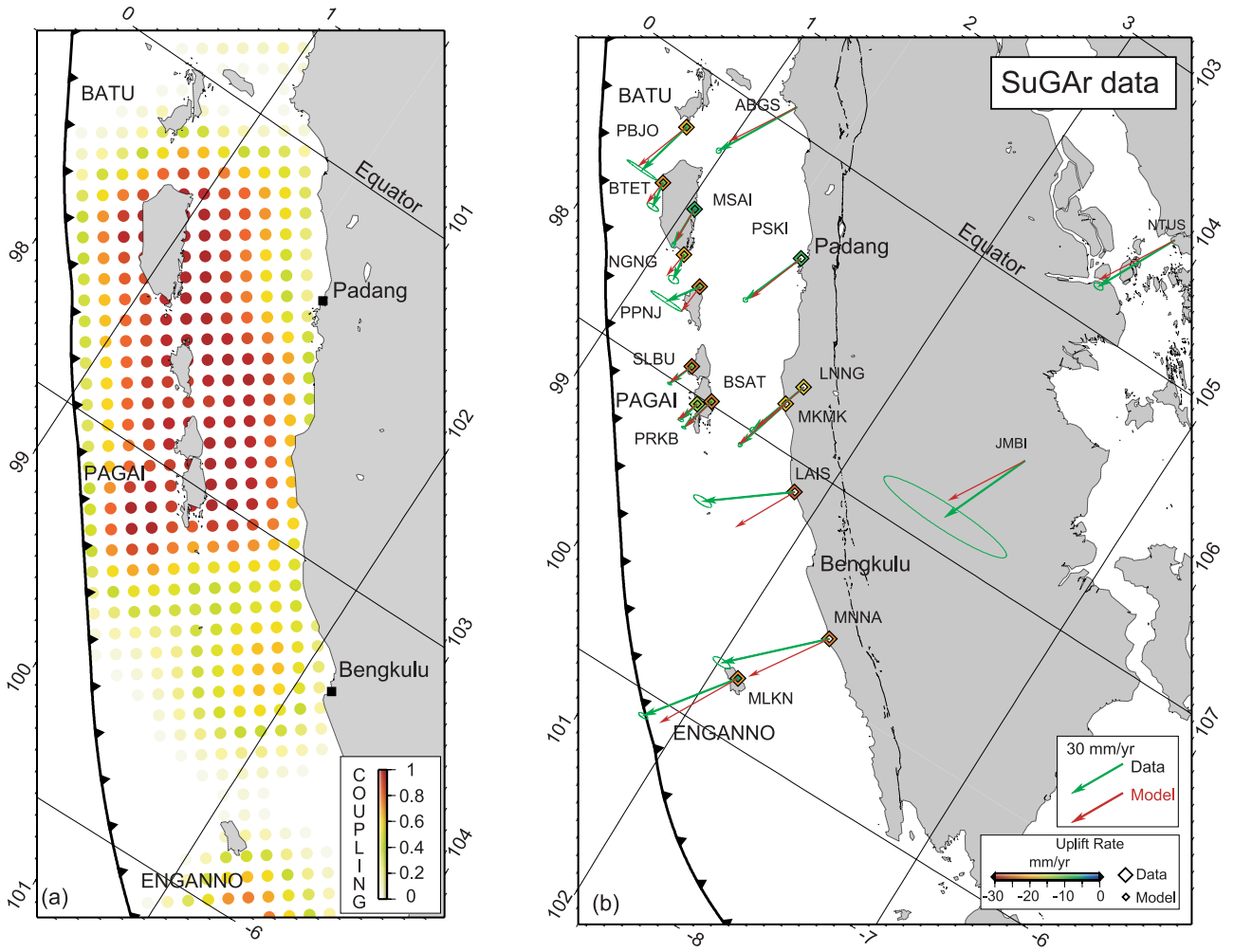

Figure 9. Distribution of coupling on the Sumatra megathrust derived from the formal inversion of the horizontal velocities and uplift rates derived from the CGPS measurements at the SuGAr stations (processed at SOPAC). To reduce the influence of postseismic deformation caused by the March 2005 Nias-Simeulue rupture, velocities were determined for the period between June 2005 and October 2006. (a) Distribution of coupling on the megathrust. Fully coupled areas are red and fully creeping areas are white. This model reveals strong coupling beneath the Mentawai Islands (Siberut, Sipora, and Pagai islands), offshore Padang city, and suggests that the megathrust south of Bengkulu city is creeping at the plate velocity. (b) Comparison of observed (green) and predicted (red) velocities. The χ_r^2 associated to that model is 24.5 (Table 8).

[46] The discrepancy between the fully locked limit and the cumulative moment deficit curves since 1700 A.D. shows that aseismic creep, integrated over all parts of the megathrust above 40 km, must account for 14% to 43% of the activity of the megathrust. If the remainder of the activity must be seismic, then 86% to 57% of the slip on the megathrust occurs during earthquakes. This corresponds to a mean interseismic coupling ratio of 0.57 to 0.86 at depths less than 40 km. In fact, however, the amount of seismic slip has been much less than this.

[47] Figure 11 displays estimates of cumulative seismic moment released over the same period, based on studies of historical seismicity [*Newcomb and McCann*, 1987], paleogeodetic analyses of major historical events [*Natawidjaja et al.*, 2006], geodetic analyses of the 2005 Nias-Simeulue earthquake [*Briggs et al.*, 2006; *Konca et al.*, 2007] and preliminary source models of the M_w 8.4 and M_w 7.9 earthquakes of 2007 (Table 9). Over the 300-year period, seismic slip accounts for merely 21% to 41% of megathrust slip at depths shallower than 40 km. This disparity implies an average 'seismic coupling' coefficient between 0.21 and 0.41 for this entire section. This low value is due in part to the fact that in many places the megathrust is not fully locked during the interseismic period, but seems too small to balance interseismic deficit of moment (or equivalently of slip). Interseismic accumulation and seismic release balance only if one assumes the maximum moments for seismic ruptures and near-minimum estimates of interseismic moment deficit accumulation.

[48] It is improbable that the misfit results only from the incompleteness of the catalog or from systematic underestimate of the seismic moment. Other large historical earth-

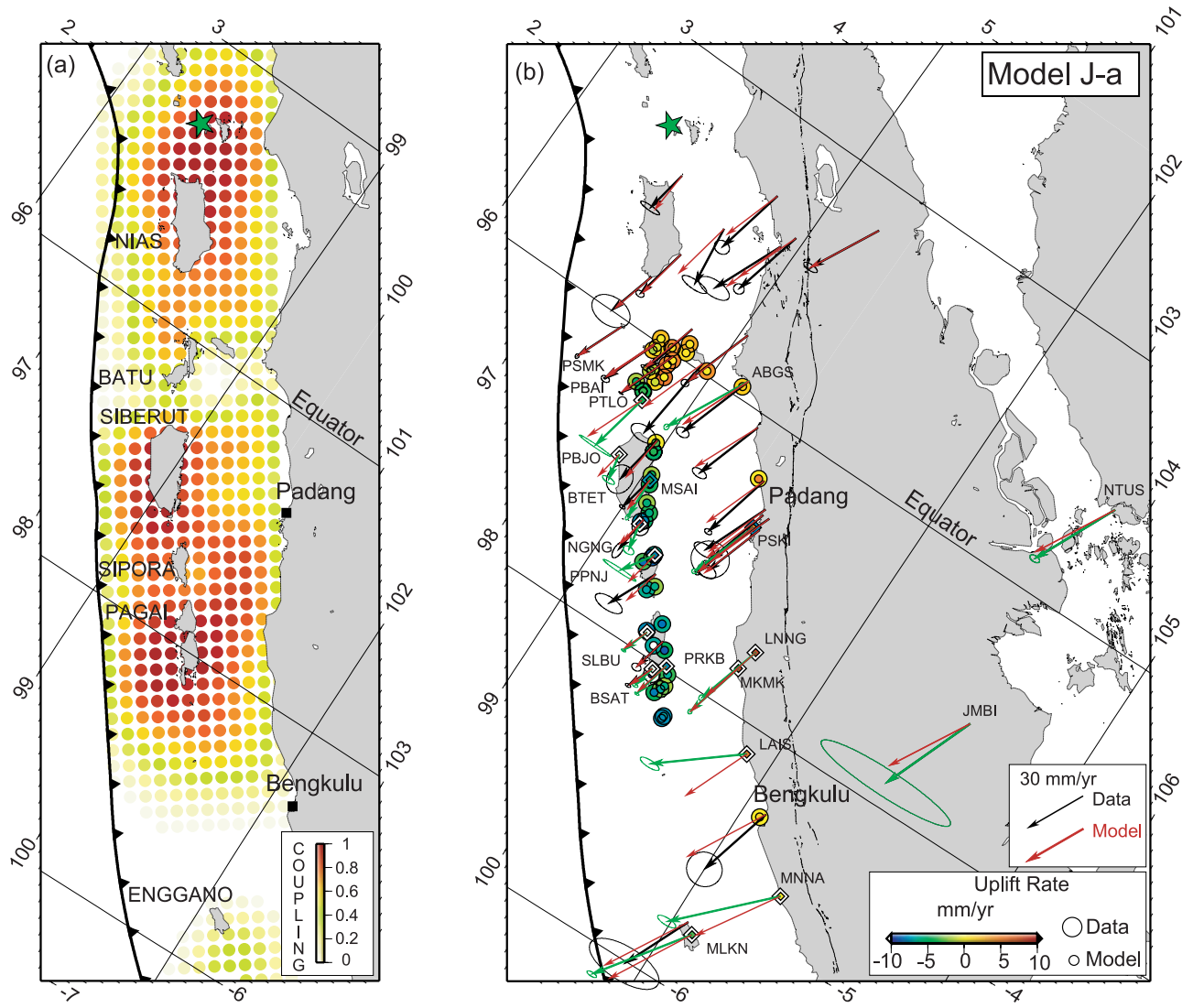

Figure 10. Distribution of coupling on the Sumatra megathrust derived from the formal inversion of all the data (model J-a, Table 8). (a) Distribution of coupling on the megathrust. Fully coupled areas are red, and fully creeping areas are white. This model shows strong coupling beneath Nias island and beneath the Mentawai (Siberut, Sipora and Pagai) islands. The rate of accumulation of moment deficit is 4.5×10^{20} N m/a. (b) Comparison of observed (black arrows for pre-2004 Sumatra-Andaman earthquake and green arrows for post-2005 Nias earthquake) and predicted velocities (in red). Observed and predicted vertical displacements are shown by color-coded large and small circles (for the corals) and large and small diamonds (for the CGPS), respectively. The χ^2_r of this model is 12.8.

quakes are known, but they are clearly smaller than those of 1861, 1833 and 1797. One plausible explanation is that strain accumulation and relief do not balance over just a few hundred years and, thus, the past three centuries might not be long enough to represent the long-term average seismicity. It was shown that for Japan, the seismic record needed to be at least 400 years long for seismic release to balance strain accumulation [*Wesnousky et al.*, 1984].

[49] Another possibility is that the pattern and rates of interseismic coupling over the past half century might not be representative of the past three centuries. We have reason to suspect that this is the case, since there is evidence in the corals for a large (M_w 8.4) transient aseismic event beneath the Mentawai and Batu islands in 1962 [*Natawidjaja et al.*, 2007]. However, about eleven rapid aseismic slip events as large as this would be required over the past three centuries to completely explain the discrepancy.

[50] Another plausible explanation for the discrepancy is that the earthquakes of 2005 and 2007 are the beginning of a rapid sequence of large seismic ruptures. Another one to two earthquakes the size of the 1833 earthquake would bring seismic release into approximate balance with interseismic accumulation.

5.2. Heterogeneous Coupling Along Strike and Its Relationship to Seismic Behavior

[51] The rate of accumulation of moment deficit varies markedly both along strike and downdip (Figures 6, 8, 9,

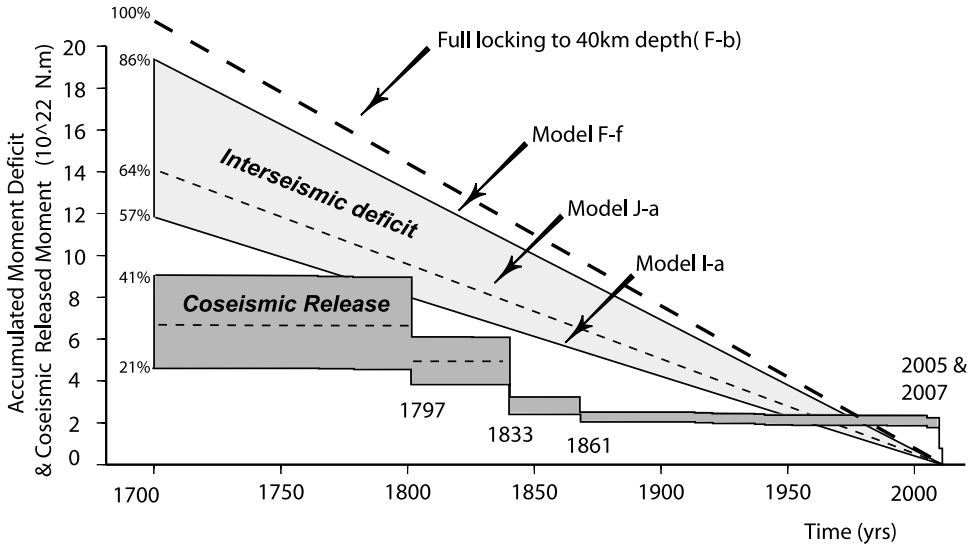

Figure 11. Accumulated moment deficit and seismic moment released due to major intraplate earthquakes between latitudes 2°N and 6°S since 1700. The accumulated moment deficit rates are predicted from model F-f (Table 5 and Figure 6c) and from the inversion models I-a (Table 7 and Figure 8) and J-a (Table 8 and Figure 10). The accumulated moment deficit rate of model F-b with a uniform 150-km width lateral coupling (Table 5) is shown for reference. Moments released for the 1797 and 1833 events are updated from *Natawidjaja et al.* [2006], the 2005 Nias-Simeulue earthquake is from *Konca et al.* [2007] and are all listed with others in Table 9. The average coseismic released moment (dashed line) divided by the average accumulated moment deficit provides a seismic coupling coefficient between 0.21 and 0.41 over the last 300 years.

and 10). Consider first simply the variations along strike for both end-members models F-f and I-a (Figure 12). We constructed this plot from the average values of rate of moment accumulation by summation within 0.5° wide swaths centered along profiles drawn perpendicular to the trench. The region of greatest similarity in the two models is between 3°S and 2°N. This reach, where the models are best constrained (see Appendix B), includes both a region of low coupling (beneath the Batu islands, near the equator) and regions of high coupling (beneath Nias island and the Mentawai islands of Siberut, Sipora, and North and South Pagai). The models diverge appreciably farther north and south, where data are much more sparse and where the resolution is poor (Appendix B).

[52] The section of narrow locking and low coupling has not produced great earthquakes ($M_w > 8.0$), whereas the sections that have a wide zone of locking and high coupling have generated $M_w > 8.5$ earthquakes (Figures 13a and 13b). In particular, the patch that produced the M_w 8.7 earthquake of March 2005 coincides well with the wide patch of high coupling below and surrounding Nias island. The southern edge of the 2005 rupture extends slightly into the predominantly decoupled equatorial patch.

[53] Near the equator, the forward models suggest a narrow locked fault zone at depths between about 20 and 35 km (Figure 13a); the inverse models imply coupling ratios near zero at depths greater than 35 km and a coupling ratio less than 0.6 at shallower depths (Figure 13b). The low interseismic coupling there is consistent with the fact

Table 9. Characteristics of Major Interplate Earthquakes on the Sunda Megathrust Offshore Sumatra[a]

Date	M_w	Released Moment, 10^{21} N m	References
1797	8.7–8.9	7.5–30	revised from *Natawidjaja et al.* [2006]
1833	8.9–9.1	10–55	revised from *Natawidjaja et al.* [2006]
1861	8.3–8.5	4.1–7.5	*Newcomb and McCann* [1987]
1935	7.7	0.33	*Natawidjaja et al.* [2004] and *Rivera et al.* [2002]
2000	7.9	1.23	*Abercrombie et al.* [2003]
2004	9.1–9.2	65–70	*Ammon et al.* [2005], *Chlieh et al.* [2007], and *Vigny et al.* [2005]
2005	8.6–8.7	9.8–12.4	*Briggs et al.* [2006], *Hsu et al.* [2006], and *Konca et al.* [2007]
2007	8.4		http://www.tectonics.caltech.edu/slip_history/index.html http://earthquake.usgs.gov/eqcenter/eqinthenews/2007/us2007hear/finite_fault.php
2007	7.9	1.0–1.1	http://www.tectonics.caltech.edu/slip_history/index.html http://earthquake.usgs.gov/eqcenter/eqinthenews/2007/us2007hear/finite_fault.php

[a]See location in Figure 1. These characteristics were determined from paleogeodetic data [*Natawidjaja et al.*, 2006, 2004] or historical accounts [*Newcomb and McCann*, 1987]. Only one third (0.46×10^{21} N m) of the total moment released by the M_w 7.9 earthquake of 2000 was accommodated by thrusting on the megathrust [*Abercrombie et al.*, 2003]. For the 2004 and 2005 events, afterslip accrued the coseismic moment by as much as 25%, essentially during the first year following these earthquakes [*Chlieh et al.*, 2007; *Hsu et al.*, 2006]. Some similar amount of postseismic moment could be included in the moment assigned to the 1797 and 1833 earthquakes given that these were determined from paleogeodetic data.

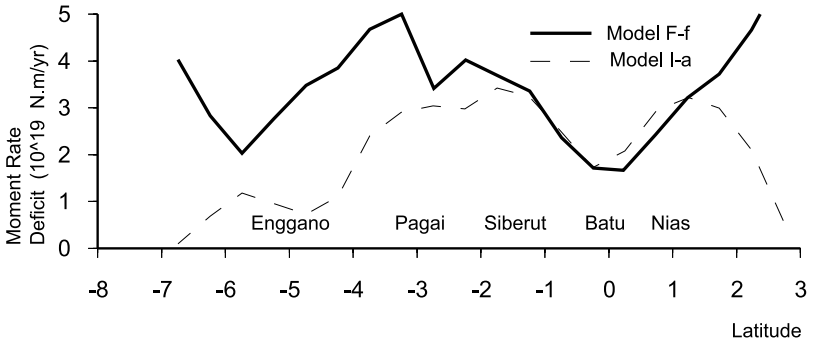

Figure 12. Latitudinal distribution of the accumulated moment deficit rate corresponding to models F-f (Table 5) and I-a (Table 7), which we consider to bracket the range of possible values. The values represent integrals over half a degree of latitude. These two models provide upper and lower bounds to the rate of accumulation of moment deficit. Their similarity in the central portion of the study area, between 2°N and 3°S, shows that coupling is well constrained by the data set. Farther north and south, where the data coverage is sparse, coupling is poorly constrained.

that this segment of the Sumatra megathrust is known to have produced only moderate earthquakes. The largest earthquake there in 260 years was a M_w 7.7 event in 1935 which resulted from megathrust failure at depths between 15 and 27 km [*Natawidjaja et al.*, 2004; *Rivera et al.*, 2002]. Paleogeodetic uplift associated with the 1935 rupture and historical seismograms confine its source within the narrow locked patch in models F-f and J-a. Other recent large earthquakes were caused by rupture of portions of the equatorial patch in 1984 (M_w 7.2) and 1998 (M_w 7.0) at similar depths. The sections of the megathrust both updip and downdip of this seismic patch seem to be slipping aseismically. The low degree of coupling is also consistent with coral evidence that shows that, like the great 2005 rupture, none of the great historical earthquake ruptures to the south (in 1797 and 1833) or to the north (in 1861) penetrated significantly into this region. This region of low megathrust coupling is directly above the subducting Investigator Fracture Zone and a well-defined concentration of seismicity within the downgoing slab [*Fauzi et al.*, 1996; *Prawirodirdjo et al.*, 1997].

[54] The region of strong coupling between the equator and Enggano island is coincident with the great megathrust ruptures of 1797 and 1833, as deduced from the uplift of fossil corals [*Natawidjaja et al.*, 2006]. Assuming the same layered 1-D CRUST2.0 structure used in this study, a reestimation of the moment released by these two great ruptures yields respective moment magnitudes (M_w) of 8.9 to 9.1 and 8.7 to 8.9 for the 1833 and 1797 events. The northern limit of the great 1833 rupture is likely under or just north of Sipora island, in the vicinity of a less coupled patch (Figures 13a and 13b) and a region of high moderate seismicity. The southern extent of the 1833 rupture is poorly constrained, but is likely between 3.5°S and 5°S, a region through which a substantial southward increase in background seismicity, narrowing of the locked patch and a diminishment of the coupling ratio occur. The differences in detail between forward and inverse models in this region may simply reflect scant data. Uninhibited by data there, we speculate that the M_w 7.9 rupture of 2000 demarcates the southern end of the 1833 rupture.

[55] Preliminary models of the M_w 8.4 and M_w 7.9 earthquakes of September 2007 (http://www.tectonics.caltech.edu/slip_history/index.html or http://earthquake.usgs.gov/eqcenter/eqinthenews/2007/us2007hear/finite_fault.php) show that these events initiated around the edges of the highly coupled patch that last ruptured in 1833. The moment of these two events is much smaller than both the moment released in 1833 and the interseismic moment deficit accumulated since then.

[56] Uplift of fossil corals reveals that the great 1797 rupture involved failure of the megathrust beneath all the Mentawai islands [*Natawidjaja et al.*, 2006]. The northern end of the rupture was near the southernmost of the Batu islands, and the southern end was beneath South Pagai. Thus, failure of much of the wide, strongly coupled Mentawai section was involved. The northern edge of rupture coincides with the southern edge of the weakly coupled equatorial patch. The southern edge of the rupture is within the strongly coupled Mentawai patch.

[57] Sparse GPS data on Enggano island and near Bengkulu show that the megathrust in this vicinity is only slightly coupled, like the equatorial patch (Figures 6c, 8, 9, and 10). This is a region of many major but no great earthquakes, the most recent being the M_w 7.9 earthquake of 2000, caused by rupture of both the megathrust and a strike-slip fault within the subducting slab [*Abercrombie et al.*, 2003].

[58] The strong correlation between historical great earthquakes and patches of the megathrust that are currently strongly coupled implies that patches that break during large megathrust events are persistent features that accumulate moment deficit during the interseismic period. Likewise, those patches beneath the Batu Islands and Enggano may characterized by lesser and narrower coupling over periods of time much greater than a century or two. If so, they may commonly serve as barriers inhibiting the lateral propagation of great earthquake ruptures.

5.3. Comparing Seismic Moment and Slip With Interseismic Moment Deficit and Slip Deficit Accumulation

[59] Having established that wide locked patches correlate with great megathrust ruptures and that narrow

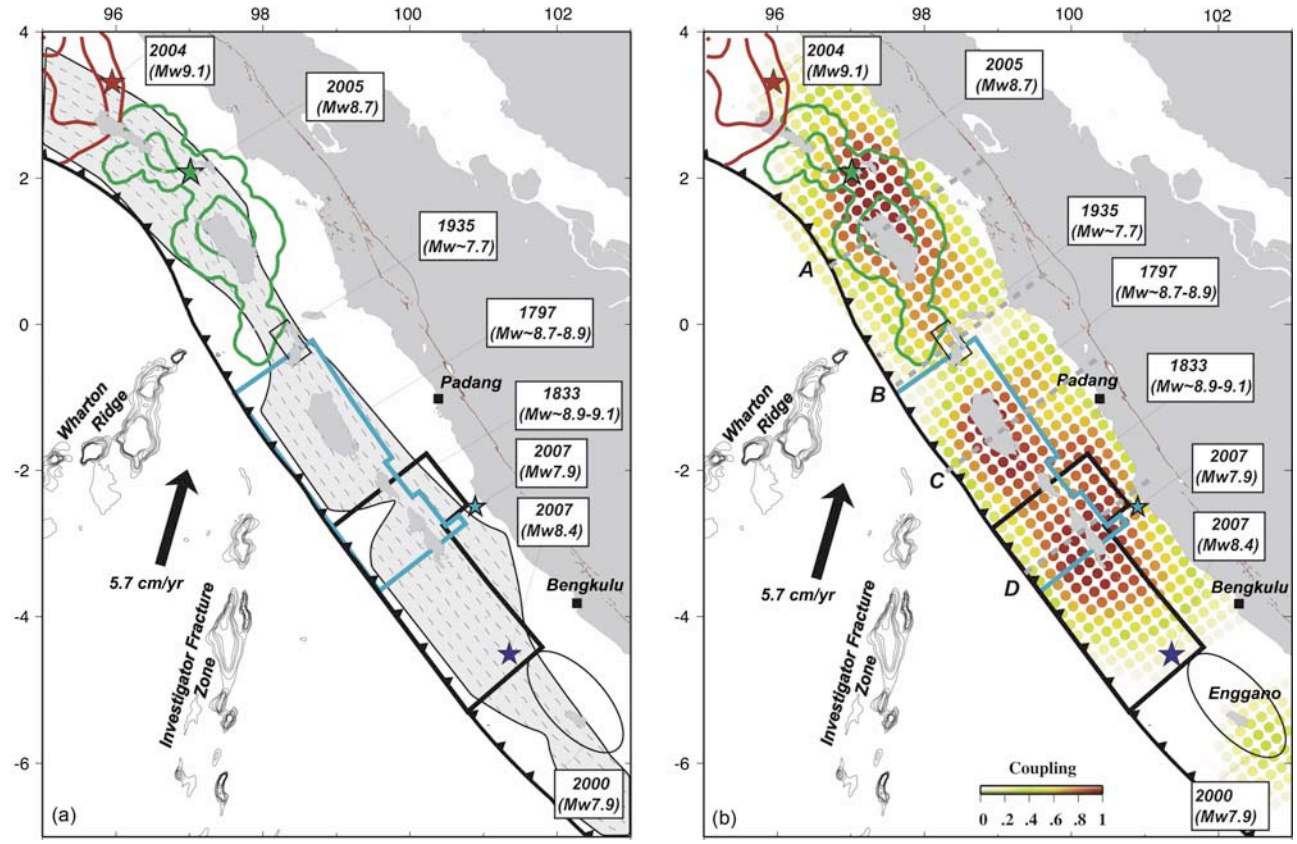

Figure 13. Comparison of interseismic coupling along the megathrust with the rupture areas of the great 1797, 1833, and 2005 earthquakes. The southernmost rupture area of the 2004 Sumatra-Andaman earthquake lies north of our study area and is shown only for reference. Epicenters of the 2007 M_w 8.4 and M_w 7.9 earthquakes are also shown for reference. (a) Geometry of the locked fault zone corresponding to forward model F-f (Figure 6c). Below the Batu Islands, where coupling occurs in a narrow band, the largest earthquake for the past 260 years has been a M_w 7.7 in 1935 [*Natawidjaja et al.*, 2004; *Rivera et al.*, 2002]. The wide zones of coupling, beneath Nias, Siberut, and Pagai islands, coincide well with the source of great earthquakes ($M_w > 8.5$) in 2005 from *Konca et al.* [2007] and in 1797 and 1833 from *Natawidjaja et al.* [2006]. The narrow locked patch beneath the Batu islands lies above the subducting fossil Investigator Fracture Zone. (b) Distribution of interseismic coupling corresponding to inverse model J-a (Figure 10). The coincidence of the high coupling area (orange-red dots) with the region of high coseismic slip during the 2005 Nias-Simeulue earthquake suggests that strongly coupled patches during interseismic correspond to seismic asperities during megathrust ruptures. The source regions of the 1797 and 1833 ruptures also correlate well with patches that are highly coupled beneath Siberut, Sipora, and Pagai islands.

locked patches correspond to smaller seismic ruptures, we now compare the amount of moment released in those earthquakes with the spatial distribution of accumulated moment deficit. Figure 14 compares the latitudinal distribution of moment released by large megathrust earthquakes and the deficit of moment accumulated since the historical earthquakes of 1797, 1833, and 1861. It shows that the segments with higher rates of interseismic moment deficit accumulation also produce higher seismic moment release.

[60] Consider first the region of the 2005 Nias-Simeulue earthquake. Figures 14a and 14b show that the sum of coseismic and postseismic moment of the 2005 event is appreciably smaller than the moment deficit accumulated since the previous rupture, in 1861. Figure 15a shows how the deficit of slip accumulated since 1861, computed from model J-a, compares with the 2005 coseismic and postseismic slip [*Hsu et al.*, 2006; *Konca et al.*, 2007]. The 2005 rupture equaled or exceeded 145 years of accumulated slip deficit in the region of peak slip but fell short of the accumulated deficit both updip and downdip, or when integrated values are considered. The local overshoot of 2005 may not really exist, however, since the less peaked character of the interseismic curve may reflect the fact that data constraining it are much sparser. If we assume that the magnitude of the 1861 event is $M_w \sim 8.3–8.5$, as estimated by *Newcomb and McCann* [1987], our analysis shows that the deficit of moment accumulated since then exceeds the moments of either the 2005 or 1861 event. Because the accumulated moment deficit since 1861 seems significantly larger than the moment released in 1861 and in 2007, neither the slip-

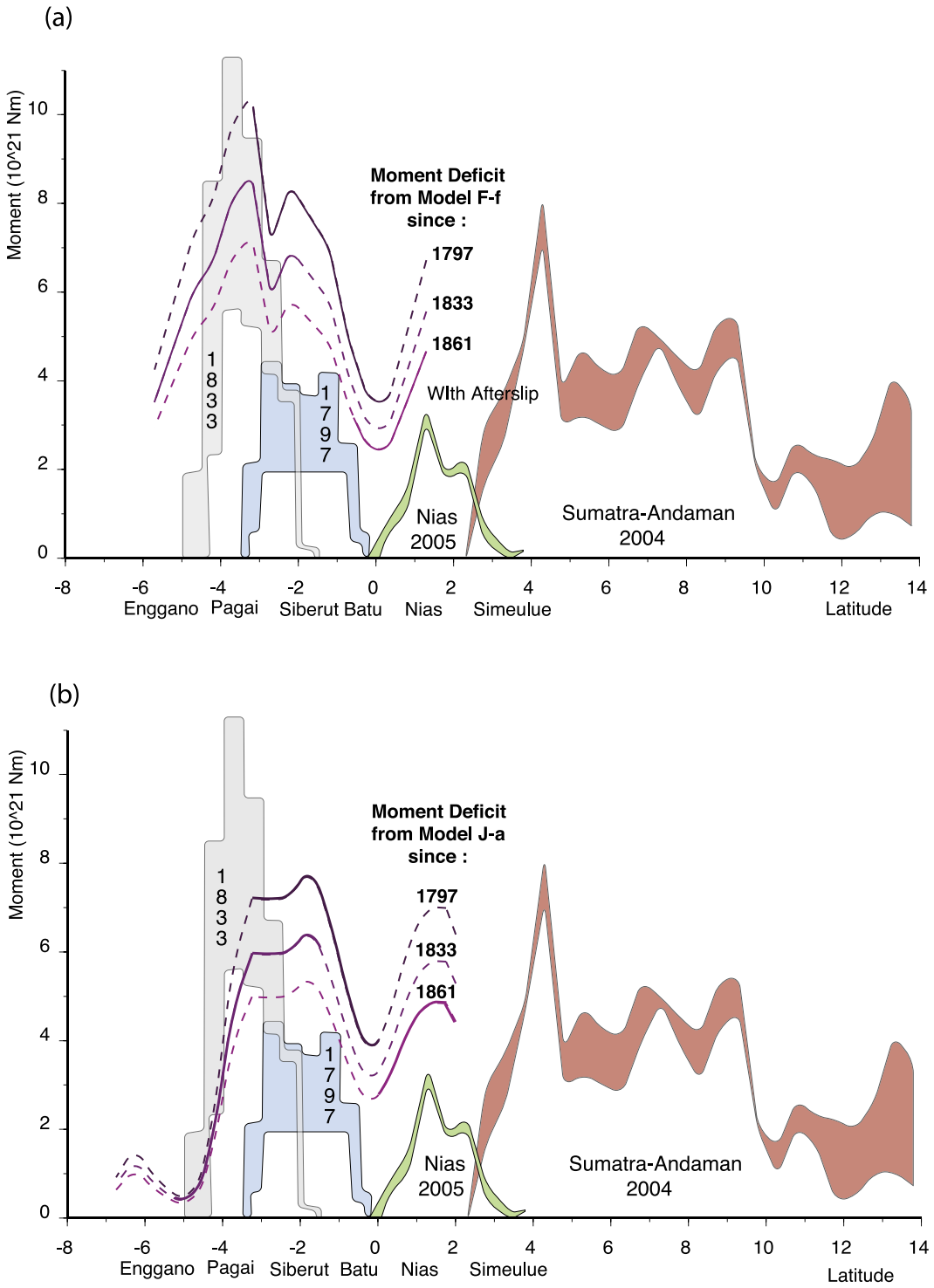

Figure 14. Latitudinal distributions of seismic moment released by great historical earthquakes and of accumulated deficit of moment due to interseismic locking of the plate interface. Values represent integrals over half a degree of latitude. Accumulated interseismic deficits since 1797, 1833, and 1861 are based on (a) model F-f and (b) model J-a. Seismic moments for the 1797 and 1833 Mentawai earthquakes are estimated based on the work by *Natawidjaja et al.* [2006], the 2005 Nias-Simeulue earthquake is taken from *Konca et al.* [2007], and the 2004 Sumatra-Andaman earthquake is taken from *Chlieh et al.* [2007]. Postseismic moments released in the month that follows the 2004 earthquake and in the 11 months that follows the Nias-Simeulue 2005 earthquake are shown in red and green, respectively, based on the work by *Chlieh et al.* [2007] and *Hsu et al.* [2006].

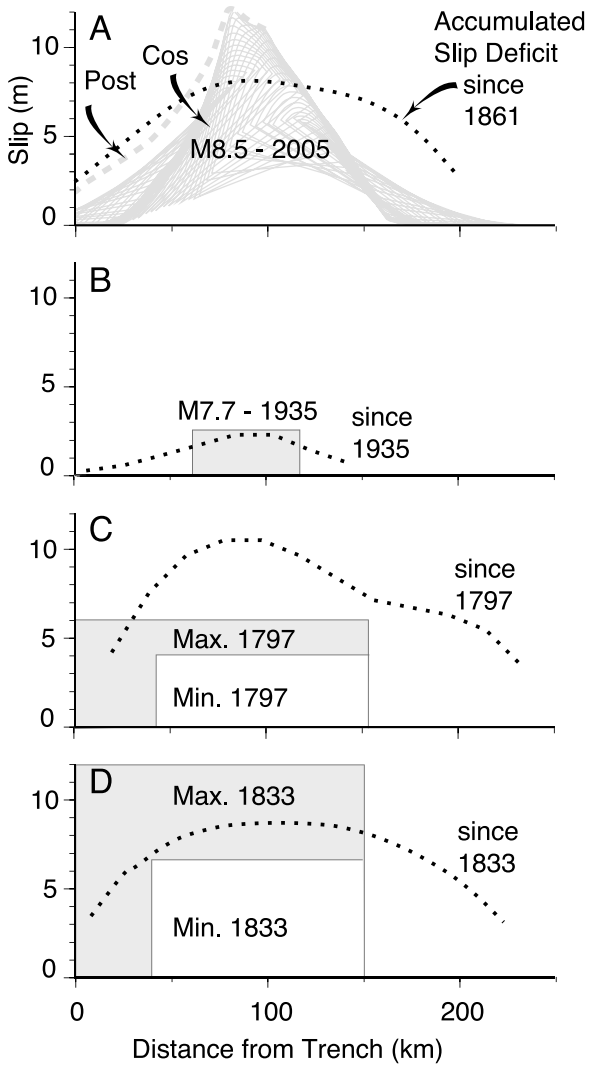

Figure 15. Downdip profiles that allow comparison of slip during large earthquakes with interseismic slip deficits of model J-a (see profiles in Figure 13b). (a) Published slip in 2005 across Nias segment. The slip has a higher, narrower peak than the slip deficit that we infer to have accumulated since the previous great earthquake, in 1861 (see section 5.3 for more details). (b) Similarly, slip inferred from coral paleoseismology to have occurred during the M_w 7.7 earthquake of 1935. The slip is nearly equal to slip accumulated across the Batu islands in the 70 years since that event. (c) Slip inferred from coral paleoseismology to have occurred beneath Siberut island in 1797. The slip is less than what we infer to have accumulated since that earthquake. (d) Slip inferred to have occurred beneath South Pagai island in 1833. The slip is 100 to 200% of the amount that has accumulated since the earthquake.

predictable nor the time-predictable model [*Shimazaki and Nakata*, 1980] seem to apply in this particular case.

[61] In the region of the equatorial patch the downdip peak in interseismic slip deficit correlates well with the area of seismic slip in 1935 (Figure 15b). It is surprising, though, that the slip deficit that has accumulated since the M_w 7.7 rupture of 1935 nearly equals the amount of slip that occurred during that earthquake, because it suggests that rerupture of this patch could happen again soon, even though the paleoseismic record shows that the last sudden failure of the patch occurred at least 138 years prior to 1935. Perhaps the interseismic slip deficit was accumulating at a much lower rate in the two centuries prior to 1935, or perhaps balancing of accumulation and release occurs over more than one earthquake cycle and return periods are extremely irregular.

[62] Moment deficit accumulated along the northern part of the Mentawai segment since 1797 is also significantly larger than what was released during that earthquake. Even if we include the moment associated with the M_w 8.4 aseismic event of 1962, the discrepancy persists. Across Siberut island, the slip deficit that has accumulated since 1797 (Figure 15c) appears to be up to twice as great as the slip that is estimated to have occurred during that earthquake. This is consistent with the observation that the corals uplifted in 1797, have returned today to their pre-1797 level [*Natawidjaja et al.*, 2007]. These observations are the origin of the concern that the next major failure of the northern part of the Mentawai section may be imminent.

[63] The southern part of the Mentawai section, from about 2°S to 4°S, last ruptured in 1833. The interseismic moment deficit that has accumulated since then is somewhat smaller than what was released in 1833. The interseismic moment deficit accumulation calculated from the inverse model (Figure 14b) is 30 to 55% of the 1833 event, and the accumulation calculated from the forward model (Figure 14a) is about 75% of the 1833 event. The latter calculation is more consistent with field observations: Interseismic subsidence of coral heads raised out of the water in 1833 now equals about 80% of the coseismic uplift. Thus, it appears that the southern section of the Mentawai locked patch is well advanced in its seismic cycle, if sequential seismic ruptures are similar in size.

5.4. What Controls Coupling Along the Plate Interface?

[64] The fact that modern strongly coupled patches of the megathrust correspond to patches that have produced great earthquakes over the past two centuries implies that the pattern of megathrust coupling is a persistent feature. Some authors have pointed to the correlation between fore-arc structures and seismic asperities, the location of maximum seismic moment released during large interplate earthquakes [*Song and Simons*, 2003; *Wells et al.*, 2003]. More precisely, it seems that the seismic moment release is generally highest beneath fore-arc basins and local gravity lows. No such correlation is observed here. Quite to the contrary, we observe that the most strongly coupled patches and seismic asperities correlate with the largest outer arc islands (Figures 13a and 13b). Even though the pattern of coupling and the location of major seismic asperities have a completely different association than in those previous studies, our conclusion is the same–the persistence of coupled patches and seismic aperities must be due to persistent properties of the megathrust.

[65] A common view is that temperature and lithological variations are key factors in megathrust behavior

[*Hyndman and Peacock*, 2003; *Hyndman and Wang*, 1993]. For example, the change from stick-slip to stable sliding may be coincident with intersection of the megathrust with the fore-arc Moho. Below the Moho, megathrusts may creep due to serpentinization of the mantle wedge above the megathrust [*Oleskevich et al.*, 1999]. Serpentine, a common product of hydrated ultramafic rocks, is indeed a rate-strengthening material that promotes stable sliding [*Reinen et al.*, 1991]. In the Sumatran case, however, the Mentawai section of the megathrust seems to extend significantly deeper than the fore-arc Moho, whose depth is probably less than 30 km [*Simoes et al.*, 2004]. Furthermore, gravity data suggest little lateral variation in depth of the fore-arc Moho [*Grevemeyer and Tiwari*, 2006]. Thus, it is probably not the cause of the lateral variation of the downdip extent of the locked fault zone.

[66] Perhaps, instead, the variations we see in downdip locking depth are due to along-strike variations in temperature. The onset of stable sliding of quartzo-feldspathic rocks like the sediments being subducted with the Australian plate, is likely between 300°C and 400°C [*Blanpied et al.*, 1991; *Blanpied et al.*, 1995]. If the temperature of the downdip edge of the locked fault zone falls within this temperature range, it would imply that temperature is the predominant control on downdip locking depth of the megathrust. At first glance this is an attractive hypothesis, because the subducting Australian plate increases in age (and hence cools) southward (Figure 16a). The observed increase in depth of locking between the equator and ~4°S is consistent with that trend. It is also consistent with the southward increase in locking depth and the southward increase in convergence rate (Figure 2). This implies that isotherms on the megathrust should plunge southward to deeper levels.

[67] To assess this possibility, we have estimated the temperature along the plate interface from modeling of 2-D sections assumed to be in steady state (Figure 16). The model takes into account the southward increase in both the convergence rate and the age of the subducting oceanic plate (see Appendix C for details on the computation). If the 300–400°C isotherms control the downdip edge of the locked fault zone, the southern increase of the age of the subducting plate affects the depth of locked fault zone by 7 to 13 km (Appendix C, Figure C1a) for a uniform convergence rate of 44 mm/a. The southern increase of the trench-normal convergence rate may increase the depth of the locked fault zone only by 2 to 7 km for a uniform 56 Ma subducting plate (Appendix C, Figure C1b). Together the lateral variations of these two parameters partially explain the southward increase of the downdip edge of locked fault zone from the Batu islands, where it is 35 km deep to South Pagai island, where it reaches a depth of about 55 km (Figure 16b).

[68] The lack of data between the islands and the trench makes it difficult to assess the updip extent of the locked fault zone over most of the study area. However, the shallowest portion of the plate interface does appear to be creeping in three places: updip of Nias, Batu, and Sipora islands. Shallow creep must occur at a low rate or during transient episodes since this portion of the plate interface lies in the stress shadow of deeper locked asperities. Transient aseismic slip updip of the Nias-Simeulue earthquake rupture has been documented [*Hsu et al.*, 2006].

[69] The mode of slip along this portion of the subduction interface may be governed by clay minerals that promote rate-strengthening friction. Smectite, in particular, breaks down to illite, which is rate weakening and therefore promote stick slip, by dehydration at about 100°C. Our thermal modeling shows that the 100°C isotherm is reached at about 25–35 km from the trench. This is consistent with the updip termination of seismic rupture of 2005 well before the trench, followed by appreciable afterslip immediately updip [*Hsu et al.*, 2006]. Although the geodetic and paleogeodetic data do not provide tight constraints on the shallowest portions of the megathrust, it seems that the lateral variation in depth of the updip portion of the locked fault zone does not follow a particular isotherm.

[70] Clearly, temperature cannot explain all the variations of coupling we observe. Creep on the shallow portion of the megathrust depends not only on its frictional properties, hence on temperature, but also on the driving shear stresses, which varies through the seismic cycle [*Bürgmann et al.*, 2005; *Wang and Dixon*, 2004]. Where the megathrust is strongly coupled, shallow afterslip may only occur in the early postseismic phase, as was observed after the Nias earthquake. Where coupling is low, shallow slip might occur throughout the interseismic period, because the stress shadow effect is presumably not as effective. This might be happening in the Batu Islands area, where low coupling could be related to the subduction of the Investigator Fracture Zone (Figures 13a and 13b). Fracture zones are generally thought to be the loci of intense hydration, hence serpentinization, of ultramafic rocks on the subducting plate. If subduction of the Investigator Fracture Zone beneath the Batu islands places serpentine against the megathrust, it would encourage aseismic slip on the megathrust.

[71] The low coupling between about 4°S and 6°S, south of Pagai island, where intense seismic activity occurred in the last 15 years [*Abercrombie et al.*, 2003], does not appear to be related to of a fracture zone nor to the thermal structure. The cause for the low coupling there remains enigmatic.

6. Conclusions

[72] Paleogeodetic (1962–2000) and geodetic (1991–2004) measurements of interseismic deformation along the Sumatra subduction zone show a heterogeneous pattern of coupling along the plate interface. The plate interface creeps at the plate convergence rate at depths greater than about 55 km, but is partially or fully locked at shallower depths. The rupture areas of large megathrust earthquakes correlate well with patches of high coupling. This suggests that asperities are long-lived features caused by intrinsic local properties of the megathrust. Even after the two great earthquakes of December 2004 and March 2005, the pattern of coupling in the Mentawai islands inferred from the SuGAr GPS data in the period June 2005 to October 2006 (Figure 9a) is remarkably similar

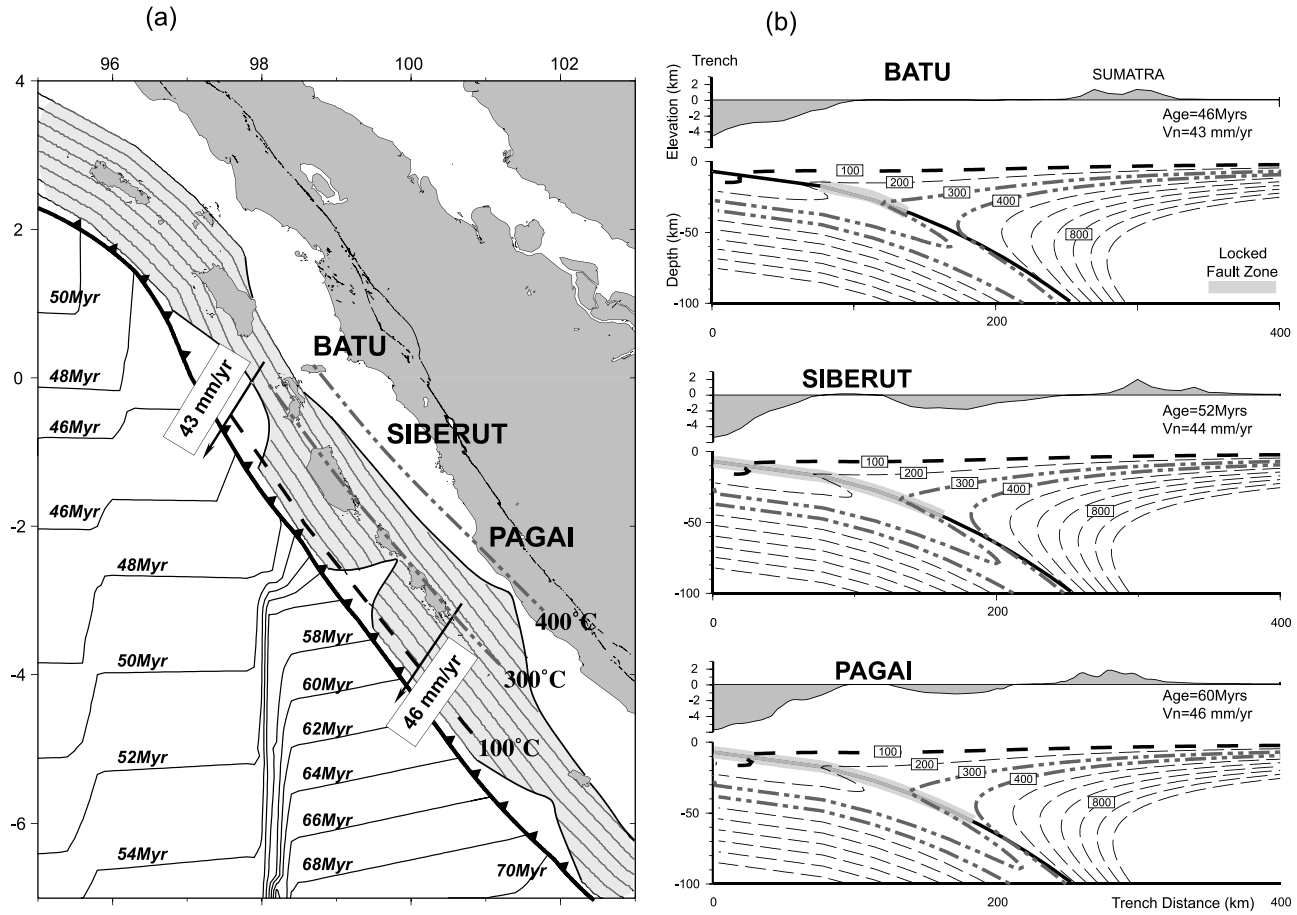

Figure 16. Thermal evolution on the megathrust interface as function of depth. (a) Map view of 100°C, 300°C, and 400°C isotherms, as deduced from thermal modeling, superposed on locked fault zone of model F-f. The lateral variations of the age of the subducting oceanic plate are indicated in Ma [*Cande and Kent*, 1995; *Gradstein et al.*, 1994]. (b) Topographic and steady state thermal structure of the megathrust for trench-normal sections across the Batu, Siberut, and Pagai islands. The locked fault zone of the megathrust deduced from model F-f is reported in gray with contour lines each 5 km depth. Isotherms are computed from analytical expression of the steady state thermal structure model [*Royden*, 1993]. The model accounts for conduction, advection, a shear heating of 40 mW/m^2 (corresponding to a friction coefficient of 0.1), and upper plate radiogenic heat production of 0.4 mW/m^3. The two parameters varying between profiles are the age and the normal convergence velocity of the subducting plate (see Appendix C for more details). On each profile, the downdip end of the locked fault zone appears to be in the range between 300°C and 400°C. However, temperature is probably not the only, nor the main, cause of the lateral variation of coupling.

to the pattern of coupling inferred from the pre-2004 geodetic and paleogeodetic data (Figure 8a).

[73] The various physical factors controlling the long-term behavior of the Sumatran section of the Sunda megathrust remain unclear. Temperature might play a role in governing the coupling, but it can only account for slight variations in the depth of downdip and updip edges of the locked fault zone. Other factors must also contribute to the lateral variations we have documented. This could include the effect of structures on the subducting plate (in particular, the Investigator Fracture Zone). Temporal variations of shear stress on the shallow portion of the megathrust due to a stress shadow effect [*Bürgmann et al.*, 2005; *Wang and Dixon*, 2004] may also play a role, but correspondence of patches of strong coupling with large interplate ruptures and the morphology of the fore arc demonstrate that the heterogeneity of coupling most probably results from properties of the megathrust that persist far longer than one or even several earthquake cycles.

[74] Our study demonstrates that the Nias-Simeulue earthquake resulted from rupture of a portion of the megathrust that is strongly coupled. The seismic moment of the earthquake and the afterslip in the first several months are somewhat smaller than the deficit of moment that had accumulated since the previous rupture of that segment in 1861.

[75] Farther south, enough moment deficit has accumulated since the great 1797 and 1833 earthquakes that the occurrence of great earthquakes in the near future seems inescapable. Moments of the M_w 8.4 and 7.9

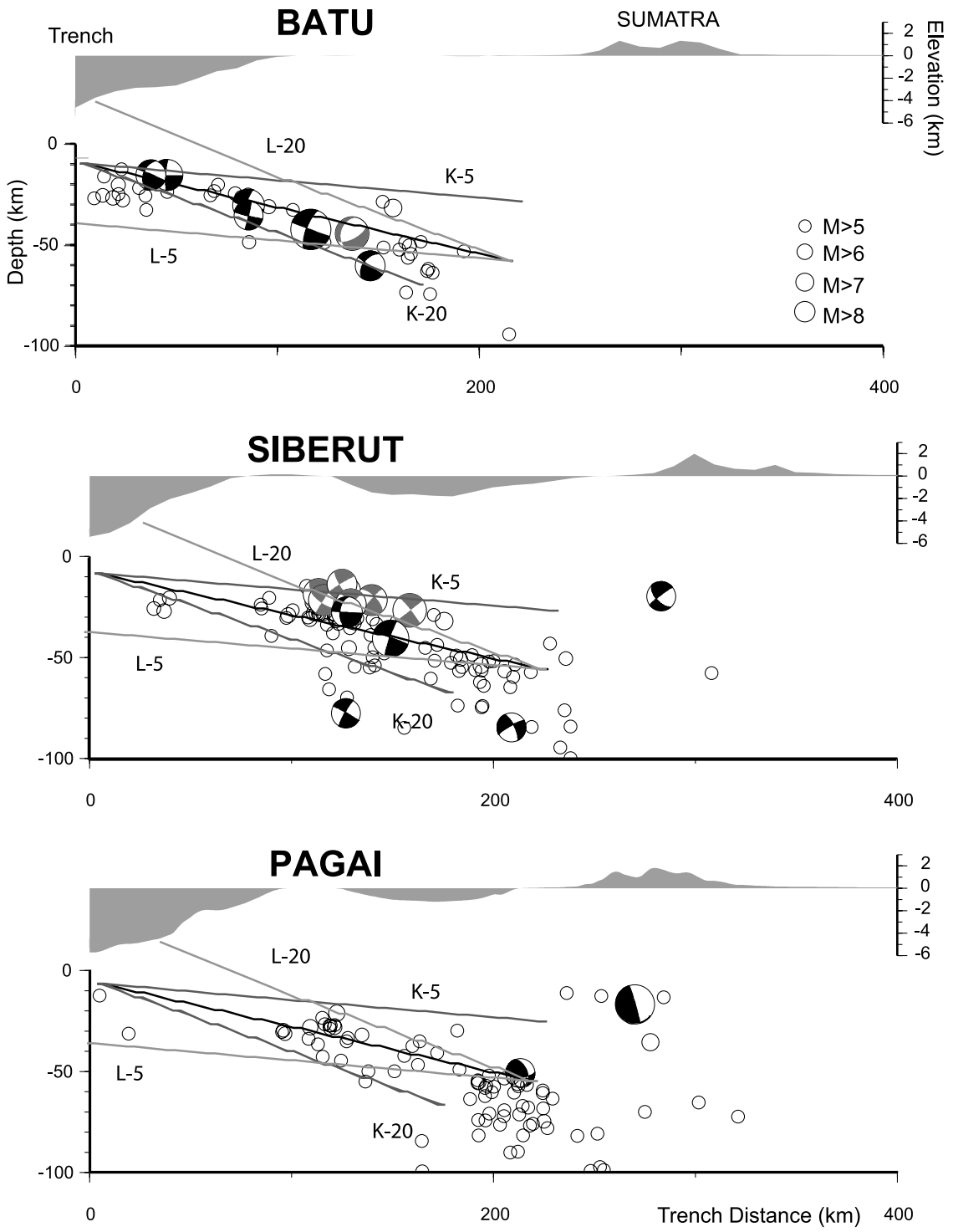

Figure A1. Sensitivity tests for variable megathrust geometry. The geometry is constrained to meet either the trench (series K) or a fixed downdip edge set at a depth of 55 km (series L).

earthquakes of 2007 account for only a small fraction of the deficit of moment accumulated since 1833. Thus, we speculate that these recent earthquakes are the initial events in the next sequence of rupture of this segment of the megathrust. This sequential failure of the Mentawai section of the Sunda megathrust helps to complete a failure sequence that began with the great Sumatra-Andaman and Nias-Simeulue earthquake earthquakes of 2004 and 2005.

Appendix A: Sensitivity to the Assumed Megathrust Dip Angle

[76] In order to test the sensitivity of our results to the assumed geometry of the megathrust, we have computed

Table A1. Reduced χ_r^2 And Moment Deficit Accumulation Rate $\dot{M}_o$ Obtained From the Joint Inversion of the All the Geodetic and Paleogeodetic Data for Various Dip Angles and Depths of the Megathrust[a]

Inversion Models	$\dot{M}_o$, 10^{20} N m/a	Imposed Edge of Megathrust	Dip Angle	χ_r^2
K-5	1.99	trench	5°	13.5
K-10	2.39	trench	10°	12.2
K-13 = J-a	2.72	trench	13°	12.8
K-16	3.05	trench	16°	14.0
K-20	2.83	trench	20°	22.5
K-25	2.43	trench	25°	58.5
L-5	3.51	downdip edge	5°	24.6
L-10	3.13	downdip edge	10°	15.5
L-13	2.72	downdip edge	13°	12.8
L-16	2.23	downdip edge	16°	11.6
L-20	1.98	downdip edge	20°	61.3
L-25	2.00	downdip edge	25°	568.0

[a]See Figure A1. The megathrust is assumed planar and to meet either the trench or a downdip edge set at 55 km depth, about 200 km away from the trench. The moment deficit accumulation rate $\dot{M}_o$ is integrated between 2°N and 3°S where the model is well constrained.

series of models obtained from the joint inversion of all the data presented in the paper. In these models, the megathrust geometry is assumed planar, with a dip angle varying from 5° to 25°, and is constrained to meet either the trench (series K) or a fixed downdip edge (series L) set at a depth of 55 km, about 200 km away from the trench (Figure A1 and Table A1). Models K are more realistic with regard to the modeling of the shallow creeping portion of the plate interface, while models L would be more realistic to account for creep along the plate interface at depth deeper than the

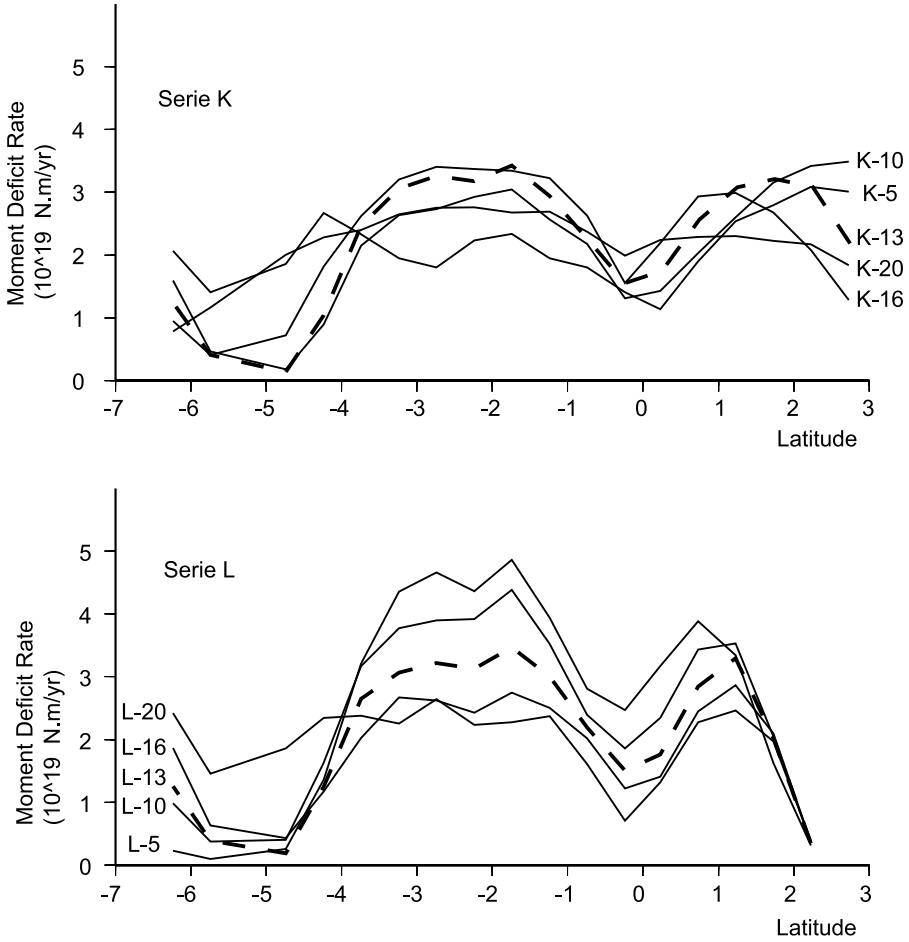

Figure A2. Latitudinal distribution of the accumulated moment deficit rate corresponding to models with geometry series K and L. The lines were drawn by summation of the moment deficit rate integrated over half a degree of latitude. The coupling is well constrained by the data set between 2°N and 3°S. The moment deficit accumulation rate $\dot{M}_o$ integrated over that region is reported in Table A1.

locked fault zone. These models explore the effect of varying both the dip angle and the depth of the megathrust. Table A1 lists the fit to the data and the rate of accumulation of moment deficit corresponding to these various models. The pattern of coupling in map view is not much sensitive to the assumed geometry and always look similar to model J-a. The fit to the data is best for a dip angle of 10° (model K-10) and degrades rapidly when a dip angle larger than about 16° is assumed for series K models. For series L models, the fit to the data is best for a dip angle of 16° (model L-16) and degrades for dip angle smaller than about 10°. The 13° dip angle assumed in the inversion models of the paper is somewhat more consistent with the dip angle of the major interplate events such as the M_w 8.7 2005, Nias earthquake, or the M_w 7.7 1935 [*Konca et al.*, 2007; *Rivera et al.*, 2002] or with the CMT of the moderate interplate events (Figure A1). The caveat is that if the plate interface is shallower (∼10°) or steeper (∼16°) than what we have assumed (13°), the rates of moment deficit accumulation might be either slightly overestimated for series K models either slightly underestimated for series L models, by maybe up to 15% (Figure A2 and Table A1).

Appendix B: Spatial Resolution of the Formal Inversion

[77] We present here checkerboard resolution tests using the inversion procedure described in section 4. We divided the megathrust interface in rectangular patches of 140 km × 80 km (Figure B1) and assigned each patch a coefficient coupling of either 1, for fully locked patches, or 0, for fully decoupled patches creeping at the plate convergence rate (Figure B1a). The synthetic model corresponds to an accumulation rate of moment deficit of $\dot{M}_o = 5.0 \times 10^{20}$ N m/a. We computed the theoretical uplift rates and horizontal velocities at all the sites where we have observations and assigned them the data uncertainties.

[78] The result of the inversion of uplift rates, using only the coral data coverage, is shown in Figure B1b. From the Mentawai to the Batu Islands the resolution is reasonably good but it drops abruptly north of the Batu and south of Pagai. The inversion yields an accumulation rate of moment deficit of 2.0×10^{20} N m/a, which represents only about 40% of the initial value.

[79] The result of the inversion of the horizontal velocities, using only the GPS data coverage, is shown in Figure B1c. It does not reveal as well as the details of the distribution of coupling below the fore-arc islands, where most coral data were collected, but it constrains the broad pattern better. It improves in particular the resolution on the Nias segment and the inversion yields an accumulation rate of moment deficit of 3.7, which is about 75% of the initial $\dot{M}_o$.

[80] When the two types of data are inversed jointly the spatial resolution is improved significantly (Figure B1d). The latitudinal distribution of accumulation rate of moment deficit is relatively well reproduced, except north of Nias (north of latitude 2°N) and between Pagai and Enggano (around latitude 3°S) where the data coverage is really poor (Figure B2).

Appendix C: Thermal Modeling

[81] We model the steady state thermal structure of the megathrust interface from analytical expressions describing the dissipative heating in the lithosphere for different rates of accretion and sedimentation to explore possible thermal control on coupling along the plate interface [*Royden*, 1993]. We adopt on the approach developed by *Royden* [1993] in which the heat transfer equation is solved in two dimensions:

$$\frac{\partial h}{\partial t} = \kappa \nabla^2 T + \nu \frac{\nabla T}{\partial z} + SH + R \qquad \text{(C1)}$$

where $\kappa \nabla^2 T$ describe the term of conduction, $\nu(\nabla T/\partial z)$ is the advection, *SH* the shear heating and *R* the crustal radiogenic production. We assume the case where the radiogenic production is small, about 0.4 μW/m^3. We neglect accretion and erosion (which need to balance each other for steady state to be possible). The shear heating is calculated for a friction coefficient of 0.1 and a uniform shear stress of 40 MPa consistent with previous value used for thermal modeling beneath the Batu Islands [*Simoes et al.*, 2004]. We fixed the temperature at the base of the oceanic lithosphere at 1300°C. For an instantaneous heating or cooling of a semi-infinite half-space, the thickness H of the subducting plate is proportional to the thermal diffusion distance $(\kappa * A)^{0.5}$:

$$H = 2.32 * (\kappa * A)^{0.5} \qquad \text{(C2)}$$

where κ is the thermal diffusivity (assumed to be equal to 1 mm^2/s), A is the age of the subducting plate [*Turcotte and Schubert*, 2002]. Following this relation, the thickness of the megathrust increases from 88 km at the Batu Islands where the oceanic plate is ∼46 Ma to 106 km south of the Pagai Islands where it is ∼66 Ma. The normal convergence rate also increases southward from about 42 to 46 mm/a over the same section (compare Figure 2).

[82] Figure C1 shows how the temperature along the plate interface varies when one or the other parameter is varied. Figures C1a and C1b reflect that for a given depth younger subducting plates are hotter, and the slower the normal convergence rate, the hotter the slab interface will be. For a given isotherm, we can estimate the contribution of each

Figure B1. (a) Checkerboard resolution tests using an initial checkerboard with elementary rectangles of 140 × 80 km^2, either fully coupled (in red) either totally creeping (white). The predicted displacements of this checkerboard are computed at each coral (blue squares) and GPS (yellow squares) sites. The results of the inversions are shown in the case where we consider (b) only the coral data, (c) only the GPS data and (d) both. The input model potency normalized by the area covered by the data is about 70% in Figure B1b and more than 90% in Figures B1c and B1d. These tests shows the good complement of the two data sets to resolve updip, intermediate, and downdip coupling from North Nias to the south Pagai islands. Out of that segment, the resolution is poor in Enggano island and totally lost at Simeulue island.

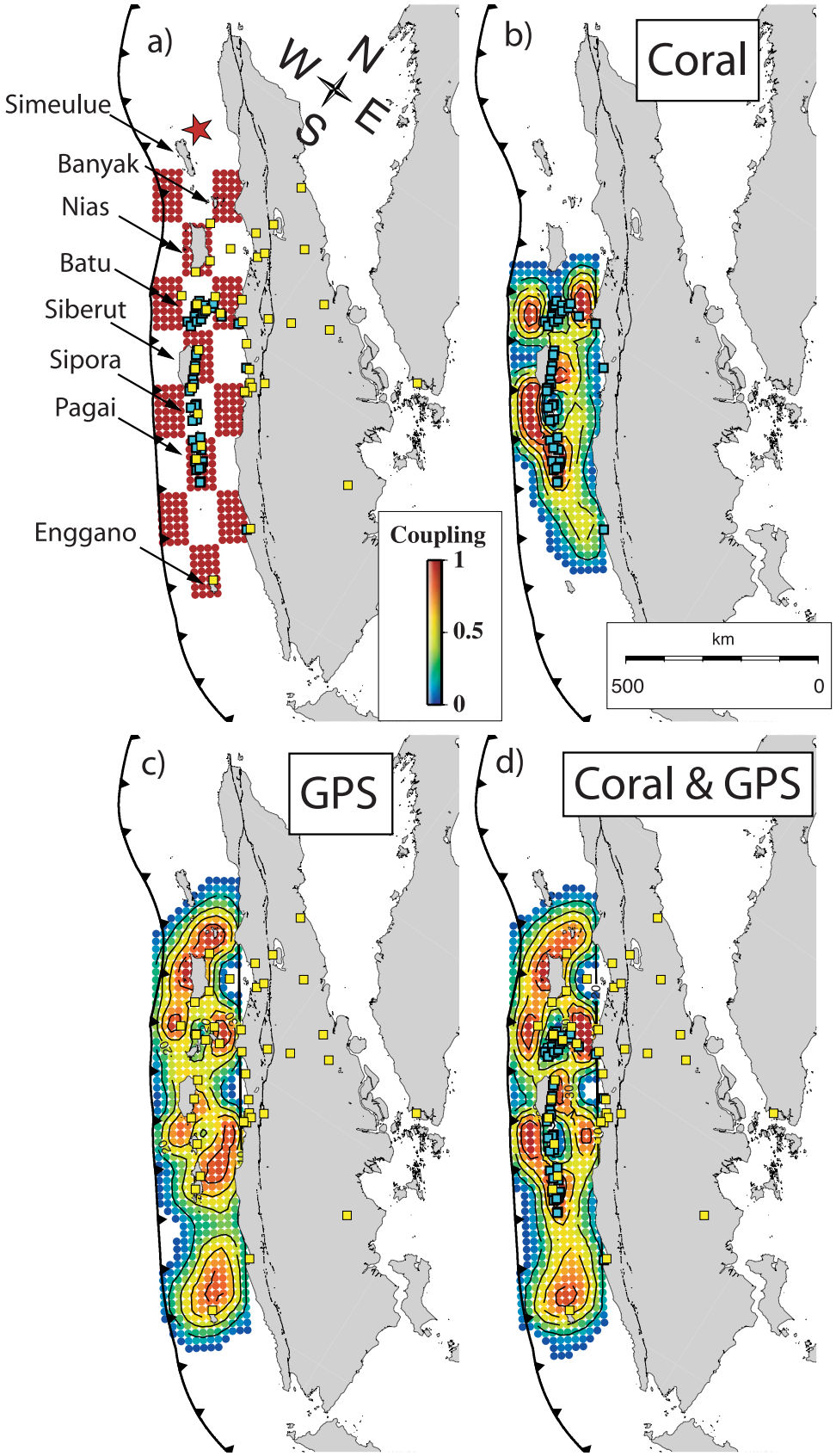
a)
b)
c)
d)
Coral
GPS
Coral & GPS
Simeulue
Banyak
Nias
Batu
Siberut
Sipora
Pagai
Enggano
W
N
S
E
Coupling
1
0.5
0
km
500
0

Figure B1

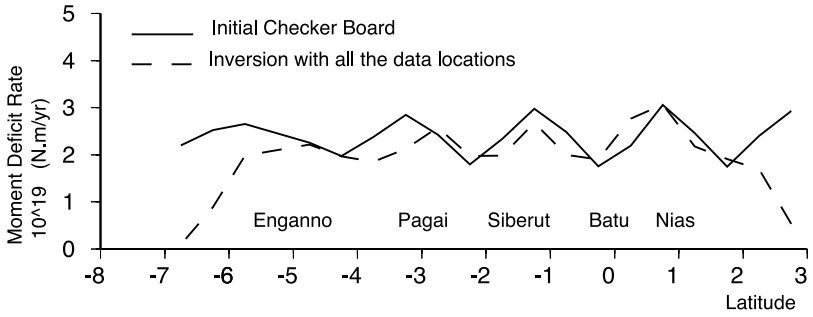

Figure B2. Comparison of the latitudinal variation of the deficit moment accumulation implies by the synthetic checkerboard model (red line, Figure B1a) and that obtained form the inversion of the predicted horizontal velocities at the GPS sites and vertical velocities at the paleogeodetic sites (black line, Figure B1d). The latitudinal distribution is relatively well reproduced, except north of latitude 2°N and between Pagai and Enggano, around latitude 3°S, where the data coverage is poor.

parameter (age and normal velocity) to increase the downdip end depth of the locked fault zone. For example, the isotherm 350°C corresponding approximately to the downdip end of the locked fault zone is 9 km deeper in the Pagai than it is in the Batu only because of the southward increase of the subducting plate age from 46 to 66 Ma (Figure C1a). In that same segment and for the same isotherm, the southward increase of normal velocity will increase the downdip end depth of the locked fault zone by about 4 km.

[83] **Acknowledgments.** Funding for this research was provided by the Gordon and Betty Moore Foundation through the Tectonics Observatory and NSF grants EAR-9628301, EAR-9804732, EAR-9903301, and EAR-0208508, administered through the NSF tectonics and geophysics programs. A RUTI IV grant from Indonesia's Ministry of Research and Technology provided support for the final phase of data analysis in 2005. Discussions with Mark Simons, Frederic Herman, Yaru Hsu, Rich Briggs,

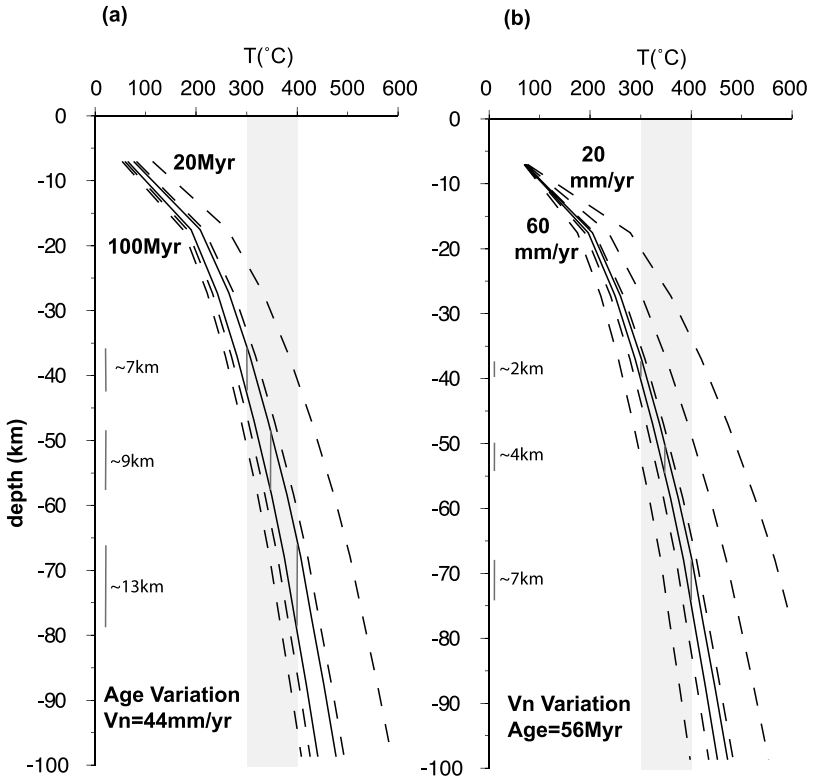

Figure C1. (a) Effect of the age on the thermal structure of the megathrust interface. The normal convergence rate is fixed to 44 mm/a, and the age is varied from 20 to 100 Ma. (b) Effect of the normal convergence rate for a 56 Ma subducting plate. The trench-normal convergence rate is varied from 20 to 60 mm/a. In Figures C1a and C1b, the range variations of these two parameters (age and normal convergence rate) from the Batu to the South Pagai of islands are indicated by the plain black lines.

and Aron Meltzner were very helpful. Use of the continuous GPS data from the Sumatran GPS Array (SuGAr) has been possible because of the efforts of all those who have worked to create and maintain the array and to collect and process its data stream, especially Bambang Suwargadi, Linette Prawirodirdjo, and Yehuda Bock. Thanks also to Anny Cazenave and DoMinh Kien for fruitful discussions on temporal sea level changes. This is Caltech Tectonics Observatory contribution 68.

References

Abercrombie, R. E., M. Antolik, and G. Ekström (2003), The June 2000 M_w 7.9 earthquakes south of Sumatra: Deformation in the India–Australia Plate, *J. Geophys. Res.*, *108*(B1), 2018, doi:10.1029/2001JB000674.

Altamimi, Z., P. Sillard, and C. Boucher (2002), ITRF2000: A new release of the International Terrestrial Reference Frame for earth science applications, *J. Geophys. Res.*, *107*(B10), 2214, doi:10.1029/2001JB000561.

Ammon, C. J., et al. (2005), Rupture process of the 2004 Sumatra-Andaman earthquake, *Science*, *308*, 1133–1139, doi:10.1126/science.1112260.

Aoki, Y., and C. H. Scholz (2003), Interseismic deformation at the Nankai subduction zone and the Median Tectonic Line, southwest Japan, *J. Geophys. Res.*, *108*(B10), 2470, doi:10.1029/2003JB002441.

Banerjee, P., et al. (2005), The size and duration of the Sumatra-Andaman earthquake from far-field static offsets, *Science*, *308*, 1769–1772, doi:10.1126/science.1113746.

Bassin, C., G. Laske, and G. Masters (2000), The current limits of resolution for surface wave tomography in North America, *Eos Trans. AGU*, *81*(48), Fall Meet. Suppl., Abstract S12A-03.

Bellier, O., and M. Sebrier (1995), Is the slip rate variation on the Great Sumatran fault accommodated by fore-arc stretching?, *Geophys. Res. Lett.*, *22*, 1969–1972, doi:10.1029/95GL01793.

Blanpied, M. L., et al. (1991), Fault stability inferred from granite sliding experiments at hydrothermal conditions, *Geophys. Res. Lett.*, *18*, 609–612, doi:10.1029/91GL00469.

Blanpied, M. L., et al. (1995), Frictional slip of granite at hydrothermal conditions, *J. Geophys. Res.*, *100*, 13,045–13,064, doi:10.1029/95JB00862.

Bock, Y., L. Prawirodirdjo, J. F. Genrich, C. W. Stevens, R. McCaffrey, C. Subarya, S. S. O. Puntodewo, and E. Calais (2003), Crustal motion in Indonesia from Global Positioning System measurements, *J. Geophys. Res.*, *108*(B8), 2367, doi:10.1029/2001JB000324.

Briggs, R. W., et al. (2006), Deformation and slip along the Sunda megathrust during the great Nias-Simeulue earthquake of March 2005, *Science*, *311*, 1897–1901, doi:10.1126/science.1122602.

Bürgmann, R., M. G. Kogan, G. M. Steblov, G. Hilley, V. E. Levin, and E. Apel (2005), Interseismic coupling and asperity distribution along the Kamchatka subduction zone, *J. Geophys. Res.*, *110*, B07405, doi:10.1029/2005JB003648.

Cande, S. C., and D. V. Kent (1995), Revised calibration of the geomagnetic polarity timescale for the late Cretaceous and Cenozoic, *J. Geophys. Res.*, *100*, 6093–6095, doi:10.1029/94JB03098.

Cazenave, A., and R. S. Nerem (2004), Present-day sea level change: Observations and causes, *Rev. Geophys.*, *42*, RG3001, doi:10.1029/2003RG000139.

Chlieh, M., et al. (2004), Crustal deformation and fault slip during the seismic cycle in the north Chile subduction zone, from GPS and InSAR observations, *Geophys. J. Int.*, *158*, 695–711, doi:10.1111/j.1365-246X.2004.02326.x.

Chlieh, M., et al. (2007), Coseismic slip and afterslip of the great (M_w 9.15) Sumatra-Andaman earthquake of 2004, *Bull. Seismol. Soc. Am.*, *97*, S152–S173, doi:10.1785/0120050631.

Church, J. A., and N. J. White (2006), A 20th century acceleration in global sea-level rise, *Geophys. Res. Lett.*, *33*, L01602, doi:10.1029/2005GL024826.

Cross, R. S., and J. T. Freymueller (2007), Plate coupling variation and block translation in the Andreanof segment of the Aleutian arc determined by subduction zone modeling using GPS data, *Geophys. Res. Lett.*, *34*, L06304, doi:10.1029/2006GL028970.

Diament, M., et al. (1992), Mentawai fault zone off Sumatra: A new key to the geodynamics of western Indonesia, *Geology*, *20*, 259–262, doi:10.1130/0091-7613(1992)020<0259:MFZOSA>2.3.CO;2.

Dmowska, R., and L. C. Lovison (1992), Influence of asperities along subduction interfaces on the stressing and seismicity of adjacent areas, *Tectonophysics*, *211*, 23–43, doi:10.1016/0040-195(92)90049-C.

Dmowska, R., et al. (1996), Seismicity and deformation at convergent margins due to heterogeneous coupling, *J. Geophys. Res.*, *101*, 3015–3029, doi:10.1029/95JB03122.

Dragert, H., et al. (1994), Current deformation and the width of the seismogenic zone of the northern Cascadia subduction thrust, *J. Geophys. Res.*, *99*, 653–668, doi:10.1029/93JB02516.

Dragert, H., et al. (2001), A silent slip event on the deeper Cascadia subduction interface, *Science*, *292*, 1525–1527, doi:10.1126/science.1060152.

Engdahl, E., et al. (1998), Global teleseismic earthquake relocation with improved travel times and procedures for depth determination, *Bull. Seismol. Soc. Am.*, *88*, 722–743.

Fauzi, et al. (1996), Lateral variation in slab orientation beneath Toba caldera, northern Sumatra, *Geophys. Res. Lett.*, *23*, 443–446, doi:10.1029/96GL00381.

Fitch, T. J. (1972), Plate convergence, transcurrent faults and internal deformation adjacent to Southeast Asia and the western Pacific, *J. Geophys. Res.*, *77*, 4432–4460, doi:10.1029/JB077i023p04432.

Fletcher, H. J., et al. (2001), High interseismic coupling of the Alaska subduction zone SW of Kodiak island inferred from GPS data, *Geophys. Res. Lett.*, *28*(3), 443–446, doi:10.1029/2000GL012258.

Fournier, T. J., and J. T. Freymueller (2007), Transition from locked to creeping subduction in the Shumagin region, Alaska, *Geophys. Res. Lett.*, *34*, L06303, doi:10.1029/2006GL029073.

Freymueller, J. T., and J. Beavan (1999), Absence of strain accumulation in the western Shumagin segment of the Alaska subduction zone, *Geophys. Res. Lett.*, *26*, 3233–3236, doi:10.1029/1999GL008356.

Genrich, J. F., Y. Bock, R. McCaffrey, L. Prawirodirdjo, C. W. Stevens, S. S. O. Puntodewo, C. Subarya, and S. Wdowinski (2000), Distribution of slip at the northern Sumatran fault system, *J. Geophys. Res.*, *105*(B12), 28,327–28,341.

Gradstein, F. M., F. P. Agterberg, J. G. Ogg, J. Hardenbol, P. van Veen, J. Thierry, and Z. Huang (1994), A Mesozoic time scale, *J. Geophys. Res.*, *99*(B12), 24,051–24,074, doi:10.1029/94JB01889.

Grevemeyer, I., and V. M. Tiwari (2006), Overriding plate controls spatial distribution of megathrust earthquakes in the Sunda-Andaman subduction zone, *Earth Planet. Sci. Lett.*, *251*, 199–208, doi:10.1016/j.epsl.2006.08.021.

Gudmundsson, O., and M. Sambridge (1998), A regionalized upper mantle (RUM) seismic model, *J. Geophys. Res.*, *103*, 7121–7136, doi:10.1029/97JB02488.

Heki, K., and Y. Tamura (1997), Short term afterslip in the 1994 Sanriku-Haruka-Oki earthquake, *Geophys. Res. Lett.*, *24*, 3285–3288, doi:10.1029/97GL03316.

Herring, T. (2000), Global Kalman filter VLBI and GPS analysis program (GLOBK), version 5.0, Mass. Inst. of Technol., Cambridge.

Hirose, H., K. Hirahara, F. Kimata, N. Fujii, and S. Miyazaki (1999), A slow thrust slip event following the two 1996 Hyuganada earthquakes beneath the Bungo Channel, southwest Japan, *Geophys. Res. Lett.*, *26*(21), 3237–3240.

Hsu, Y.-J., et al. (2006), Frictional afterslip following the M_w 8.7, 2005 Nias-Simeuleu earthquake, Sumatra, *Science*, *312*, 1921–1926, doi:10.1126/science.1126960.

Hutton, W., et al. (2001), Slip kinematics and dynamics during and after the 1995 October 9 M_w = 8.0 Colima-Jalisco earthquake, Mexico, from GPS geodetic constraints, *Geophys. J. Int.*, *146*, 637–658, doi:10.1046/j.1365-246X.2001.00472.x.

Hyndman, R. D., and S. M. Peacock (2003), Serpentinization of the forearc mantle, *Earth Planet. Sci. Lett.*, *212*, 417–432, doi:10.1016/S0012-821X(03)00263-2.

Hyndman, R. D., and K. Wang (1993), Thermal constrains on the zone of major thrust earthquake failure: The Cascadia subduction zone, *J. Geophys. Res.*, *98*, 2039–2060, doi:10.1029/92JB02279.

Ji, C., et al. (2002), Source description of the 1999 Hector Mine, California earthquake, part I: Wavelet domain inversion theory and resolution analysis, *Bull. Seismol. Soc. Am.*, *92*, 1192–1207, doi:10.1785/0120000916.

Kanamori, H. (1977), Seismic and aseismic slip along subduction zones and their tectonic implications, in *Island Arcs and Deep Sea Trenches and Back-Arc Basins*, *Maurice Ewing Ser.*, vol. 1, edited by M. Talwani and W. C. Pitman III, pp. 163–174, AGU, Washington, D. C.

Kanamori, H. (1986), Rupture process of subduction-zone earthquakes, *Annu. Rev. Earth Planet. Sci.*, *14*, 293–322, doi:10.1146/annurev.ea.14.050186.001453.

King, R., and Y. Bock (2000), Documentation for the GAMIT GPS analysis software, release 9.94, Mass. Inst. of Technol., Cambridge.

Konca, A. O., et al. (2007), Rupture kinematics of the 2005, M_w 8.6, Nias-Simeulue earthquake from the joint inversion of seismic and geodetic data, *Bull. Seismol. Soc. Am.*, *97*, S307–S322, doi:10.1785/0120050632.

Kositsky, A. P., M. Chlieh, J. Avouac, and K. Sieh (2006), Reconstruction of fault slip using principal component analysis of paleogeodetic and geodetic time-series: Application to the Sumatran subduction zone, Indonesia, *Eos Trans. AGU*, *87*(52), Fall Meet. Suppl., Abstract G33A-0031.

Lay, T., et al. (1989), Temporal variation of large intraplate earthquakes in coupled subduction zones, *Phys. Earth Planet. Inter.*, *54*, 258–312, doi:10.1016/0031-9201(89)90247-1.

Lowry, A. R., et al. (2001), Transient fault slip in Guerrero, southern Mexico, *Geophys. Res. Lett.*, *28*, 3753–3756, doi:10.1029/2001GL013238.

Mazzotti, S., et al. (2000), Full interseismic locking of the Nankai and Japan-west Kurile subduction zones: An analysis of uniform elastic strain accumulation in Japan constrained by permanent GPS, *J. Geophys. Res.*, *105*, 13,159–13,177, doi:10.1029/2000JB900060.

McCaffrey, R. (1991), Slip vectors and stretching of the Sumatran forearc, *Geology*, *19*, 881–884, doi:10.1130/0091-7613(1991)019<0881:SVASOT>2.3.CO;2.

McCaffrey, R., et al. (2000), Strain partitioning during oblique plate convergence in northern Sumatra: Geodetic and seismologic constraints and numerical modeling, *J. Geophys. Res.*, *105*, 28,363–28,376, doi:10.1029/1999JB900362.

Michel, G. W., et al. (2001), Crustal motion and block behaviour in SE-Asia from GPS measurements, *Earth Planet. Sci. Lett.*, *187*, 239–244, doi:10.1016/S0012-821X(01)00298-9.

Natawidjaja, D. H., K. Sieh, S. N. Ward, H. Cheng, R. L. Edwards, J. Galetzka, and B. W. Suwargadi (2004), Paleogeodetic records of seismic and aseismic subduction from central Sumatran microatolls, Indonesia, *J. Geophys. Res.*, *109*, B04306, doi:10.1029/2003JB002398.

Natawidjaja, D. H., K. Sieh, M. Chlieh, J. Galetzka, B. W. Suwargadi, H. Cheng, R. L. Edwards, J.-P. Avouac, and S. N. Ward (2006), Source parameters of the great Sumatran megathrust earthquakes of 1797 and 1833 inferred from coral microatolls, *J. Geophys. Res.*, *111*, B06403, doi:10.1029/2005JB004025.

Natawidjaja, D. H., K. Sieh, J. Galetzka, B. W. Suwargadi, H. Cheng, R. L. Edwards, and M. Chlieh (2007), Interseismic deformation above the Sunda Megathrust recorded in coral microatolls of the Mentawai islands, west Sumatra, *J. Geophys. Res.*, *112*, B02404, doi:10.1029/2006JB004450.

Newcomb, K., and W. McCann (1987), Seismic history and seismotectonics of the Sunda Arc, *J. Geophys. Res.*, *92*, 421–439, doi:10.1029/JB092iB01p00421.

Nikolaidis, R. (2002), Observations of geodetic and seismic: Deformations with the Global Positioning System, thesis, Univ. of Calif., San Diego.

Okada, Y. (1992), Internal deformation due to shear and tensile faults in a half-space, *Bull. Seismol. Soc. Am.*, *82*, 1018–1040.

Oleskevich, D. A., et al. (1999), The updip and downdip limits to great subduction earthquakes: Thermal and structural models of Cascadia, south Alaska, SW Japan, and Chile, *J. Geophys. Res.*, *104*, 14,965–14,991, doi:10.1029/1999JB900060.

Pacheco, J. F., et al. (1993), Nature of seismic coupling along simple plate boundaries of the subduction type, *J. Geophys. Res.*, *98*, 14,133–14,159, doi:10.1029/93JB00349.

Park, S.-C., and J. Mori (2007), Are asperity patterns persistent? Implication from large earthquakes in Papua New Guinea, *J. Geophys. Res.*, *112*, B03303, doi:10.1029/2006JB004481.

Prawirodirdjo, L., et al. (1997), Geodetic observations of interseismic strain segmentation at the Sumatra subduction zone, *Geophys. Res. Lett.*, *24*, 2601–2604, doi:10.1029/97GL52691.

Prawirodirdjo, L., et al. (2000), One century of tectonic deformation along the Sumatran fault from triangulation and GPS surveys, *J. Geophys. Res.*, *105*, 28,343–28,361, doi:10.1029/2000JB900150.

Pritchard, M. E., and M. Simons (2006), An aseismic slip pulse in northern Chile and along-strike variations in seismogenic behavior, *J. Geophys. Res.*, *111*, B08405, doi:10.1029/2006JB004258.

Reinen, L. A., et al. (1991), The frictional behaviour of serpentinite: Implications for aseismic creep on shallow crustal faults, *Geophys. Res. Lett.*, *18*, 1921–1924, doi:10.1029/91GL02367.

Rhie, J., et al. (2007), Slip of the 2004 Sumatra-Andaman earthquake from joint inversion of long-period global seismic waveforms and GPS static offsets, *Bull. Seismol. Soc. Am.*, *97*, S115–S127, doi:10.1785/0120050620.

Rivera, L., et al. (2002), A comparative study of the Sumatran subduction-zone earthquakes of 1935 and 1984, *Bull. Seismol. Soc. Am.*, *92*, 1721–1736, doi:10.1785/0120010106.

Royden, L. H. (1993), The steady state thermal structure of eroding orogenic belts and accretionary prisms, *J. Geophys. Res.*, *98*, 4487–4507, doi:10.1029/92JB01954.

Ruff, L. J., and H. Kanamori (1983), Seismic coupling and uncoupling at subduction zones, *Tectonophysics*, *99*, 99–117, doi:10.1016/0040-1951(83)90097-5.

Savage, J. C. (1983), A dislocation model of strain accumulation and release at a subduction zone, *J. Geophys. Res.*, *88*, 4983–4996.

Shimazaki, K., and T. Nakata (1980), Time-predictable recurrence model for large earthquakes, *Geophys. Res. Lett.*, *7*, 279–282, doi:10.1029/GL007i004p00279.

Sieh, K., and D. Natawidjaja (2000), Neotectonics of the Sumatran fault, Indonesia, *J. Geophys. Res.*, *105*, 28,295–28,326, doi:10.1029/2000JB900120.

Sieh, K., et al. (1999), Crustal deformation at the Sumatra subduction zone revealed by coral data, *Geophys. Res. Lett.*, *26*, 3141–3144, doi:10.1029/1999GL005409.

Simoes, M., J. P. Avouac, R. Cattin, and P. Henry (2004), The Sumatra subduction zone: A case for a locked fault zone extending into the mantle, *J. Geophys. Res.*, *109*, B10402, doi:10.1029/2003JB002958.

Simons, W. M. F., et al. (1999), Observing plate motions in South East Asia: Geodetic results of the GEODYSSEA Project, *Geophys. Res. Lett.*, *26*, 2081–2084, doi:10.1029/1999GL900395.

Simons, W. J. F., et al. (2007), A decade of GPS in Southeast Asia: Resolving Sundaland motion and boundaries, *J. Geophys. Res.*, *112*, B06420, doi:10.1029/2005JB003868.

Socquet, A., C. Vigny, N. Chamot-Rooke, W. Simons, C. Rangin, and B. Ambrosius (2006), India and Sunda plates motion and deformation along their boundary in Myanmar determined by GPS, *J. Geophys. Res.*, *111*, B05406, doi:10.1029/2005JB003877.

Song, T.-R. A., and M. Simons (2003), Large trench-parallel gravity variations predict seismogenic behavior in subduction zones, *Science*, *301*, 630–633, doi:10.1126/science.1085557.

Subarya, C., et al. (2006), Plate-boundary deformation associated with the great Sumatra-Andaman earthquake, *Nature*, doi:10.1038/nature04522.

Thatcher, W. (1990), Order and diversity in the modes of Circum-Pacific earthquake recurrence, *J. Geophys. Res.*, *95*, 2609–2623, doi:10.1029/JB095iB03p02609.

Tichelaar, B. W., and L. J. Ruff (1993), Depth of seismic coupling along subduction zones, *J. Geophys. Res.*, *98*, 2017–2037, doi:10.1029/92JB02045.

Turcotte, D. L., and G. Schubert (2002), *Geodynamics*, 2nd ed., Cambridge Univ. Press, Cambridge, UK.

Vergne, J., et al. (2001), On the use of dislocations to model interseismic strain and stress build-up at intracontinental thrust faults, *Geophys. J. Int.*, *147*, 155–162, doi:10.1046/j.1365-246X.2001.00524.x.

Vigny, C., et al. (2005), Insight into the 2004 Sumatra-Andaman earthquake from GPS measurements in Southeast Asia, *Nature*, *436*, 201–206, doi:10.1038/nature03937.

Wallace, L. M., and J. Beavan (2006), A large slow slip event on the central Hikurangi subduction interface beneath the Manawatu region, North Island, New Zealand, *Geophys. Res. Lett.*, *33*, L11301, doi:10.1029/2006GL026009.

Wallace, L. M., J. Beavan, R. McCaffrey, and D. Darby (2004), Subduction zone coupling and tectonic block rotations in the North Island, New Zealand, *J. Geophys. Res.*, *109*, B12406, doi:10.1029/2004JB003241.

Wang, K., and T. Dixon (2004), "Coupling" semantics and science in earthquake research, *Eos Trans. AGU*, *85*(18), 180, doi:10.1029/2004EO180005.

Wang, K., R. Wells, S. Mazzotti, R. D. Hyndman, and T. Sagiya (2003), A revised dislocation model of interseismic deformation of the Cascadia subduction zone, *J. Geophys. Res.*, *108*(B1), 2026, doi:10.1029/2001JB001227.

Wells, R. E., R. J. Blakely, Y. Sugiyama, D. W. Scholl, and P. A. Dinterman (2003), Basin-centered asperities in great subduction zone earthquakes: A link between slip, subsidence, and subduction erosion?, *J. Geophys. Res.*, *108*(B10), 2507, doi:10.1029/2002JB002072.

Wesnousky, S. G., et al. (1984), Integration of geological and seismological data for the analysis of seismic hazard: A case study of Japan, *Bull. Seismol. Soc. Am.*, *74*, 687–708.

Yamanaka, Y., and M. Kikuchi (2004), Asperity map along the subduction zone in northeastern Japan inferred from regional seismic data, *J. Geophys. Res.*, *109*, B07307, doi:10.1029/2003JB002683.

Zachariasen, J. (1998), Paleoseismology and paleogeodesy of the Sumatran subduction zone: A study of vertical deformation using coral microatolls, Ph.D. thesis, 418 pp, Calif. Inst. of Technol., Pasadena.

Zachariasen, J., et al. (2000), Modern vertical deformation above the Sumatran subduction zone: Paleogeodetic insights from coral microatolls, *Bull. Seismol. Soc. Am.*, *90*, 897–913, doi:10.1785/0119980016.

Zweck, C., J. T. Freymueller, and S. C. Cohen (2002), Three-dimensional elastic dislocation modeling of the postseismic response to the 1964 Alaska earthquake, *J. Geophys. Res.*, *107*(B4), 2064, doi:10.1029/2001JB000409.

J. P. Avouac, J. Galetzka, and K. Sieh, Tectonics Observatory, Division of Geological and Planetary Sciences, California Institute of Technology, Pasadena, CA 91125, USA.

M. Chlieh, Géosciences Azur, Université de Nice Sophia-Antipolis, Institut de Recherche pour le Développement, Observatoire de la Côte d'Azur, 250 rue A. Einstein, F-06560 Valbonne, France. (chlieh@geoazur.unice.fr)

D. H. Natawidjaja, Research Center for Geotechnology, Indonesian Institute of Sciences, Komplek LIPI Gd. 70, J1, Bandung 40135, Indonesia.